UNIFIED EFFICIENT LAYERWISE THEORY FOR SMART BEAMS WITH SEGMENTED EXTENSION/SHEAR MODE, PIEZOELECTRIC ACTUATORS AND SENSORS

Santosh Kapuria and Peter Hagedorn

UNIFIED EFFICIENT LAYERWISE THEORY FOR SMART BEAMS WITH SEGMENTED EXTENSION/SHEAR MODE, PIEZOELECTRIC ACTUATORS AND SENSORS

SANTOSH KAPURIA AND PETER HAGEDORN

A unified coupled efficient layerwise theory is presented for the dynamics of smart laminated beams with surface-mounted and embedded piezoelectric actuators and sensors with arbitrary poling directions, acting in extension or shear mode. The theory considers a global third-order variation across the thickness combined with a layerwise linear variation for the axial displacement, expressed in terms of only three primary variables, and accounts for the transverse normal strain due to the electric field in the approximation for the transverse displacement. The electric potential is approximated as piecewise quadratic across sublayers. A finite element is developed which has two physical nodes with mechanical and some electric potential degrees of freedom (DOF), and an *electric node* for the electric potentials of the electroded surfaces of the piezoelectric patches. The *electric nodes* eliminate the need for imposition of equality constraints of the electric DOF on the equipotential electroded surfaces of the segmented piezoelectric elements and result in significant reduction in the number of electric DOF. The electric DOF associated with the physical nodes allow for the inplane electric field that is induced via a direct piezoelectric effect. The accuracy of the formulation is established by comparing the results with those available in literature and the 2D piezoelasticity solutions for extension and shear mode actuators, sensors and adaptive beams. The effect of segmentation of the electroded surface on the deflection, sensory potential and natural frequencies is illustrated for both extension and shear mode cases. The influence of the location of extension and shear mode actuators and sensors on the response is investigated for a hybrid mode composite beam. The effect of actuator thickness on the actuation authority is studied.

1. Introduction

Adaptive laminated structures, incorporating some surface-mounted and embedded piezoelectric patches for sensing and actuation, are now widely used in noise, vibration, acoustic, shape and position control applications. Even though the orthorhombic piezoelectric materials of symmetry class mm2 [Auld 1973] have five piezoelectric constants, namely, d_{31}, d_{32} d_{33}, d_{15}, d_{24}, most research and development efforts in this technology have generally been focused on the piezoelectric elements that are poled parallel to the applied electric field (in the thickness direction) and use only the d_{31}, d_{32} constants to use membrane strains. This is known as the extension actuation mechanism (EAM). Consequently, most of the existing refined models incorporating advanced kinematics and two-way electromechanical coupling also consider the extension mode piezoelectric elements; see, for example, the review articles of Saravanos and Heyliger [1999], Gopinathan et al. [2000] and Benjeddou [2000]. Coupled discrete layer theories (DLT)

with layerwise linear description of inplane displacements and electric potential have been presented for hybrid beams [Lee and Saravanos 1996] and plates [Saravanos et al. 1997; Lage et al. 2004]. Plagianakos and Saravanos [2005] presented a higher-order DLT for hybrid beams using layerwise quadratic and cubic variations for the inplane displacements and electric potential, respectively. These theories yield excellent accuracy, but the computational effort increases in proportion to the number of layers, which restricts their application for practical dynamics and control problems. Mixed coupled equivalent single layer (ESL) theories such as the first-order shear deformation theory (FSDT) [Saravanos 1999; Wang 2004] and refined third-order theory (TOT) [Correia et al. 2000], considering a global variation for the displacements across the entire thickness and a layerwise distribution for the electric potential, have been employed for the dynamic analysis of hybrid plates. It is now well known that since these theories do not account for the layerwise (zigzag) nature of distributions of the inplane displacements, they yield inaccurate results for moderately thick laminates and even thin laminates with strong inhomogeneity across the thickness. Vasques and Rodrigues [2005] presented a finite element formulation based on a coupled partial layerwise theory for three layer piezoelectric beams. Kapuria [2001] and Kapuria and Alam [2006] presented a coupled zigzag theory for hybrid beams, which considers a layerwise approximation for the inplane displacement, like the DLT, but the number of primary displacement variables is reduced to only three as in the ESL theories, FSDT and TOT, by enforcing the conditions on the transverse shear stresses at the top and bottom surfaces and the layer interfaces. Comparison with the two-dimensional (2D) piezoelasticity solutions have established the excellent accuracy of this theory for active and sensory dynamic response of moderately thick hybrid beams for various inhomogeneous lay-ups and boundary conditions.

The piezoelectric materials, when constrained and poled perpendicularly to the applied electric field, undergo transverse shear deformation through the d_{15}, d_{24} constants, which is known as the shear actuation mechanism (SAM). The use of shear mode actuators for adaptive structures was first investigated by Sun and Zhang [1995] who carried out a 2D finite element analysis of a plane strain adaptive beam consisting of an axially poled piezoelectric core embedded between two elastic face sheets. The results showed that the shear actuators are subjected to much lower stresses compared to the extension actuators under the same electric field. Zhang and Sun [1996] presented a *three layer sandwich* beam theory for the shear actuated laminate by modeling the face layers as classical Euler–Bernoulli beams and the central core as a Timoshenko beam, without considering the two-way electromechanical coupling. Benjeddou et al. [1997] presented a finite element (FE) formulation based on this uncoupled three-layer beam model for analysis of adaptive sandwich beams with elastic/EAM piezoelectric faces and SAM piezoelectric/elastic core. An improved FE model [Benjeddou et al. 1999] eliminating the shear locking problem was used for comparing SAM and EAM actuators for static and free vibration response [Benjeddou et al. 2000]. Raja et al. [2002; 2004] generalized the sandwich model by considering laminates (instead of single layers) for the faces and the core and by incorporating the electric DOF. The electric potential was assumed to be linear across a sublaminate (core/face). Trindade and Benjeddou [2005] extended their previous model by modeling the core with the TOT and considering the variation of the electric potential to be cubic across the core thickness and linear across the faces. It was shown that this led to a significantly stiffer response, but the results did not match with the 2D FE results. It is important to note that all the publications reported above use a three layer beam model, which is rather restrictive for modeling general laminates with EAM and SAM actuators to be placed at any arbitrary location

across the thickness. It has been observed from 2D piezoelasticity solutions that the electric potential follows a nearly quadratic variation across the thickness in extension mode piezoelectric elements [Dube et al. 1996] and a nearly cubic variation in shear mode elements [Parashar et al. 2005]. It is also well established that the assumption of a linear electric potential along the thickness can cause a significant error in the computed response [Bisegna and Caruso 2001; Sze et al. 2004; Parashar et al. 2005]. Khdeir and Aldraihem [2001; 2003] presented a closed form solution for deflection analysis of beams with shear and extension actuators employing the uncoupled FSDT and an uncoupled higher-order theory. Parashar et al. [2004] presented a coupled FSDT for the nonlinear vibration of shear actuators considering material nonlinearities.

Conventionally, the finite element models based on coupled theories consider electric DOF at the nodes. However, the piezoelectric sensing and actuating patches are always electroded with metallic coating, which makes their surfaces equipotential. To model this condition, particularly for sensing, it would be necessary to impose the constraint of equality on the electric DOF of the nodes on the same electroded surface. To avoid this tedious task, the concept of electric nodes has been used by Sze and Yao [2000], wherein the electric DOF are separated from the kinetic (physical) nodes with which only mechanical DOF are associated. It results in significant reduction in the number of electric DOF. But in this approach, as all the electric DOF are associated with electric nodes, the inplane electric fields which may be induced due to direct piezoelectric effect cannot be accounted for.

In this work, a new unified coupled efficient layerwise formulation is presented for hybrid laminated beams with surface-bonded or embedded piezoelectric actuators and sensors with arbitrary poling directions, which act in extension or shear mode. The constitutive equations of piezoelectric plane stress beams and plane strain panels with arbitrary poling direction are derived using transformation rules. The axial displacement is approximated as a third-order zigzag variation across the thickness, which is expressed in terms of only three primary displacement variables. The transverse displacement is approximated to account for the transverse normal strain due to the electric field, and the electric potential is assumed to follow a quadratic variation across sublayers, which can effectively model the observed quadratic and cubic variations in, respectively, the extension and shear mode piezoelectric elements. A novel finite element is developed consisting of two physical nodes with kinetic and some electric DOF, and an *electric node* with the electric DOF for the equipotential surfaces of the electroded piezoelectric patches. The electric nodes conveniently model the equipotential condition of electroded surfaces with significantly reduced number of electric DOF. The quadratic component of electric DOF associated with the physical nodes enable modeling the inplane electric field induced due to the direct piezoelectric effect.

2. Constitutive equations for piezoelectric beams/panels with arbitrary poling direction

The 3D linear constitutive equations of a piezoelectric orthorhombic material of class mm2 symmetry (commonly used materials PZT and PVDF belong to this class or its subset), with principal material axes x_1, x_2, x_3 and polarized along axis x_3, are given by [Auld 1973]

$$\varepsilon' = S\,\sigma' + d^{\mathrm{T}}E', \qquad D' = d\,\sigma' + \epsilon\,E'; \qquad \sigma' = C\varepsilon' - e^{\mathrm{T}}E', \qquad D' = e\,\varepsilon' + \eta\,E'. \tag{1}$$
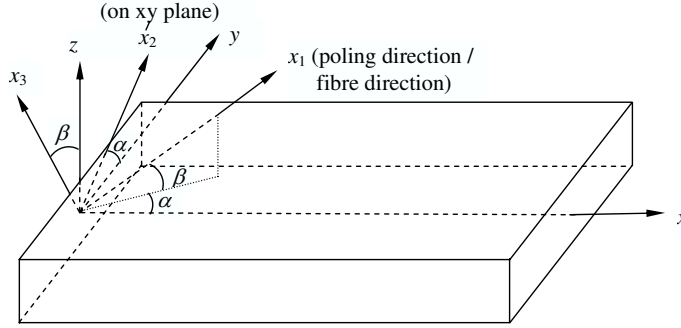
Figure 1. Reference axes (x, y, z) and material principal axes (x_1, x_2, x_3) of piezoelectric material with arbitrary poling direction.

The superscript $(\ )^{\mathrm{T}}$ denotes matrix transpose. The components of stress σ', engineering strain ε', electric field E' and electric displacement D' are given with respect to the principal material axes by

$$\sigma'=\begin{bmatrix}\sigma_1 & \sigma_2 & \sigma_3 & \tau_{23} & \tau_{31} & \tau_{12}\end{bmatrix}^{\mathrm{T}}, \ \varepsilon'=\begin{bmatrix}\varepsilon_1 & \varepsilon_2 & \varepsilon_3 & \gamma_{23} & \gamma_{31} & \gamma_{12}\end{bmatrix}^{\mathrm{T}}, \ E'=\begin{bmatrix}E_1 & E_2 & E_3\end{bmatrix}^{\mathrm{T}}, \ D'=\begin{bmatrix}D_1 & D_2 & D_3\end{bmatrix}^{\mathrm{T}}.$$

S, d, η are the matrices of elastic compliance, piezoelectric strain constants and electric permittivities, with $C = S^{-1}, e = dS^{-1}, \epsilon = \eta + ed^{\mathrm{T}}$, where

$$S = \begin{bmatrix} s_{11} & s_{12} & s_{13} & 0 & 0 & 0 \\ s_{12} & s_{22} & s_{23} & 0 & 0 & 0 \\ s_{13} & s_{23} & s_{33} & 0 & 0 & 0 \\ 0 & 0 & 0 & s_{44} & 0 & 0 \\ 0 & 0 & 0 & 0 & s_{55} & 0 \\ 0 & 0 & 0 & 0 & 0 & s_{66} \end{bmatrix}, \qquad d^{\mathrm{T}} = \begin{bmatrix} 0 & 0 & d_{31} \\ 0 & 0 & d_{32} \\ 0 & 0 & d_{33} \\ 0 & d_{24} & 0 \\ d_{15} & 0 & 0 \\ 0 & 0 & 0 \end{bmatrix}, \qquad \eta = \begin{bmatrix} \eta_{11} & 0 & 0 \\ 0 & \eta_{22} & 0 \\ 0 & 0 & \eta_{33} \end{bmatrix}.$$

Consider that the material axis x_1 is spatially oriented at angles α with the reference axis x and β with the xy-plane (Figure 1). The axis x_2 is assumed to lie on the xy-plane. Thus the poling direction x_3 is at angle β with the reference axis z which is along the thickness direction. Using transformation rules, σ, ε, E and D in the reference coordinate system (x, y, z) can be related to those in the material coordinate system (x_1, x_2, x_3) by

$$\sigma' = T\sigma, \qquad \varepsilon' = RTR^{-1}\varepsilon, \qquad D' = aD, \qquad E' = aE, \qquad (2)$$

where

$$\sigma=\begin{bmatrix}\sigma_x & \sigma_y & \sigma_z & \tau_{yz} & \tau_{zx} & \tau_{xy}\end{bmatrix}^{\mathrm{T}}, \ \varepsilon=\begin{bmatrix}\varepsilon_x & \varepsilon_y & \varepsilon_z & \gamma_{yz} & \gamma_{zx} & \gamma_{xy}\end{bmatrix}^{\mathrm{T}}, \ E=\begin{bmatrix}E_x & E_y & E_z\end{bmatrix}^{\mathrm{T}}, \ D=\begin{bmatrix}D_x & D_y & D_z\end{bmatrix}^{\mathrm{T}},$$

and the transformation matrices a, T and R are defined in the Appendix in terms of direction parameters $c = \cos\alpha$, $s = \sin\alpha$, $p = \cos\beta$, and $q = \sin\beta$. Using the transformation rules in Equation (1), the constitutive equations of a piezoelectric medium with arbitrary poling direction, with respect to reference

axes x, y, z, are obtained as

$$\varepsilon = \bar{S}\,\sigma + \bar{d}^{\mathrm{T}} E, \qquad D = \bar{d}\,\sigma + \bar{\epsilon}\,E; \qquad \sigma = \bar{C}\varepsilon - \bar{e}^{\mathrm{T}} E, \qquad D = \bar{e}\,\varepsilon + \bar{\eta}\,E, \tag{3}$$

where

$$\bar{S} = T^{\mathrm{T}} S\,T, \quad \bar{d} = a^{\mathrm{T}} d\,T, \quad \bar{\epsilon} = a^{\mathrm{T}} \epsilon\,a, \quad \bar{C} = T^{-1} C\,(T^{-1})^{\mathrm{T}}, \quad \bar{e} = a^{\mathrm{T}} e\,(T^{-1})^{\mathrm{T}}, \quad \bar{\eta} = a^{\mathrm{T}} \eta\,a.$$

For structural applications as sensors and actuators, the electric field is generally applied in the thickness direction z. Thus, for extension mode sensing/actuation mechanism, the poling direction x_3 will be along the z-axis, that is, $\beta = 0 \Rightarrow p = 1, q = 0$. For the shear mode case, the poling direction will be perpendicular to the z-axis so that $\beta = \pm 90° \Rightarrow p = 0, q = \pm 1$. Thus for extension and shear mode actuation/sensing, $pq = 0$. For this case, Equation (3) assumes the following form

$$\begin{bmatrix} \varepsilon_x \\ \varepsilon_y \\ \varepsilon_z \\ \gamma_{yz} \\ \gamma_{zx} \\ \gamma_{xy} \end{bmatrix} = \begin{bmatrix} \bar{s}_{11} & \bar{s}_{12} & \bar{s}_{13} & 0 & 0 & \bar{s}_{16} \\ \bar{s}_{12} & \bar{s}_{22} & \bar{s}_{23} & 0 & 0 & \bar{s}_{26} \\ \bar{s}_{13} & \bar{s}_{23} & \bar{s}_{33} & 0 & 0 & \bar{s}_{36} \\ 0 & 0 & 0 & \bar{s}_{44} & \bar{s}_{45} & 0 \\ 0 & 0 & 0 & \bar{s}_{45} & \bar{s}_{55} & 0 \\ \bar{s}_{16} & \bar{s}_{26} & \bar{s}_{36} & 0 & 0 & \bar{s}_{66} \end{bmatrix} \begin{bmatrix} \sigma_x \\ \sigma_y \\ \sigma_z \\ \tau_{yz} \\ \tau_{zx} \\ \tau_{xy} \end{bmatrix} + \begin{bmatrix} \bar{d}_{11} & \bar{d}_{21} & \bar{d}_{31} \\ \bar{d}_{12} & \bar{d}_{22} & \bar{d}_{32} \\ \bar{d}_{13} & \bar{d}_{23} & \bar{d}_{33} \\ \bar{d}_{14} & \bar{d}_{24} & \bar{d}_{34} \\ \bar{d}_{15} & \bar{d}_{25} & \bar{d}_{35} \\ \bar{d}_{16} & \bar{d}_{26} & \bar{d}_{36} \end{bmatrix} \begin{bmatrix} E_x \\ E_y \\ E_z \end{bmatrix},$$

$$\begin{bmatrix} D_x \\ D_y \\ D_z \end{bmatrix} = \begin{bmatrix} \bar{d}_{11} & \bar{d}_{12} & \bar{d}_{13} & \bar{d}_{14} & \bar{d}_{15} & \bar{d}_{16} \\ \bar{d}_{21} & \bar{d}_{22} & \bar{d}_{23} & \bar{d}_{24} & \bar{d}_{25} & \bar{d}_{26} \\ \bar{d}_{31} & \bar{d}_{32} & \bar{d}_{33} & \bar{d}_{34} & \bar{d}_{35} & \bar{d}_{36} \end{bmatrix} \begin{bmatrix} \sigma_x \\ \sigma_y \\ \sigma_z \\ \tau_{yz} \\ \tau_{zx} \\ \tau_{xy} \end{bmatrix} + \begin{bmatrix} \bar{\epsilon}_{11} & \bar{\epsilon}_{12} & 0 \\ \bar{\epsilon}_{12} & \bar{\epsilon}_{22} & 0 \\ 0 & 0 & \bar{\epsilon}_{33} \end{bmatrix} \begin{bmatrix} E_x \\ E_y \\ E_z \end{bmatrix}. \tag{4}$$

For a beam of small width along the direction y, a state of plane stress ($\sigma_y = \tau_{yz} = \tau_{xy} = 0$) is assumed as in [Robbins and Reddy 1991; Lee and Saravanos 1996; Plagianakos and Saravanos 2005]. We neglect transverse normal stress σ_z, that is, $\sigma_z \simeq 0$. The axial and transverse displacements u, w and electric potential ϕ are assumed to be independent of y. With these assumptions, Equation (4) reduces to

$$\begin{bmatrix} \varepsilon_x \\ \gamma_{zx} \\ D_x \\ D_z \end{bmatrix} = \begin{bmatrix} \bar{s}_{11} & 0 & \bar{d}_{11} & \bar{d}_{31} \\ 0 & \bar{s}_{55} & \bar{d}_{15} & \bar{d}_{35} \\ \bar{d}_{11} & \bar{d}_{15} & \bar{\epsilon}_{11} & 0 \\ \bar{d}_{31} & \bar{d}_{35} & 0 & \bar{\epsilon}_{33} \end{bmatrix} \begin{bmatrix} \sigma_x \\ \tau_{zx} \\ E_x \\ E_z \end{bmatrix}. \tag{5}$$

The explicit expressions of $\bar{s}_{ij}$, $\bar{d}_{ij}$ and $\bar{\epsilon}_{ij}$ in terms their values in the material coordinate system are given in the Appendix. Inversely, Equation (5) can be written as

$$\begin{bmatrix} \sigma_x \\ \tau_{zx} \\ D_x \\ D_z \end{bmatrix} = \begin{bmatrix} \hat{Q}_{11} & 0 & \hat{e}_{11} & \hat{e}_{31} \\ 0 & \hat{Q}_{55} & \hat{e}_{15} & \hat{e}_{35} \\ \hat{e}_{11} & \hat{e}_{15} & -\hat{\eta}_{11} & -\hat{\eta}_{13} \\ \hat{e}_{31} & \hat{e}_{35} & -\hat{\eta}_{13} & -\hat{\eta}_{33} \end{bmatrix} \begin{bmatrix} \varepsilon_x \\ \gamma_{zx} \\ -E_x \\ -E_z \end{bmatrix} \tag{6}$$

with

$$\hat{\eta}_{11} = \bar{\epsilon}_{11} - \hat{e}_{11}\bar{d}_{11} - \hat{e}_{15}\bar{d}_{15}, \quad \hat{\eta}_{33} = \bar{\epsilon}_{33} - \hat{e}_{31}\bar{d}_{31} - \hat{e}_{35}\bar{d}_{35}, \quad \hat{\eta}_{13} = -(\hat{e}_{31}\bar{d}_{11} + \hat{e}_{35}\bar{d}_{15}),$$
$$\hat{Q}_{11} = 1/\bar{s}_{11}, \quad \hat{Q}_{55} = 1/\bar{s}_{55}, \quad \hat{e}_{11} = \bar{d}_{11}/\bar{s}_{11}, \quad \hat{e}_{31} = \bar{d}_{31}/\bar{s}_{11}, \quad \hat{e}_{15} = \bar{d}_{15}/\bar{s}_{55}, \quad \hat{e}_{35} = \bar{d}_{35}/\bar{s}_{55}. \tag{7}$$

For infinite panels (infinite dimension along y direction), a state of plane strain exist, that is, $\varepsilon_y = \gamma_{yz} = \gamma_{xy} = 0$. For this case, with the assumption of $\sigma_z \simeq 0$, the other components of Equation (3) can be reduced to the same form as Equation (6) with the associated material constants defined as

$$\hat{\eta}_{11} = \bar{\eta}_{11} + \bar{e}_{13}^2/\bar{c}_{33}, \quad \hat{\eta}_{33} = \bar{\eta}_{33} + \bar{e}_{33}^2/\bar{c}_{33}, \quad \hat{\eta}_{13} = \bar{e}_{13}\bar{e}_{33}/\bar{c}_{33}, \quad \hat{Q}_{11} = \bar{c}_{11} - \bar{c}_{13}^2/\bar{c}_{33},$$
$$\hat{Q}_{55} = \bar{c}_{55}, \quad \hat{e}_{11} = \bar{e}_{11} - \bar{c}_{13}\bar{e}_{13}/\bar{c}_{33}, \quad \hat{e}_{31} = \bar{e}_{31} - \bar{c}_{13}\bar{e}_{33}/\bar{c}_{33}, \quad \hat{e}_{15} = \bar{e}_{15}, \quad \hat{e}_{35} = \bar{e}_{35}. \tag{8}$$

The expressions of $\bar{c}_{ij}$, $\bar{e}_{ij}$ and $\bar{\eta}_{ij}$ are given in the Appendix. Thus, Equation (6) and the subsequent development are valid for both plane stress (thin width) and plane strain (infinite panel) beams, with the material constants to be calculated using Equations (7) and (8), respectively.

3. Potential and displacement field approximations

Consider a hybrid beam having any lay-up, whose thickness h and the number of layers L may vary segment-wise due to the presence of piezoelectric patches, which can be either surface-bonded or embedded; see Figure 2. The piezoelectric patches can have the poling direction parallel or normal to the z-axis, depending on their use in extension or shear mode. The longitudinal and thickness axes are along the x and z directions. The xy-plane is chosen to be the plane which is the midplane for most of the length of the beam. Let the planes $z = z_0$ and $z = z_L$ be the bottom and top surfaces of the beam, which
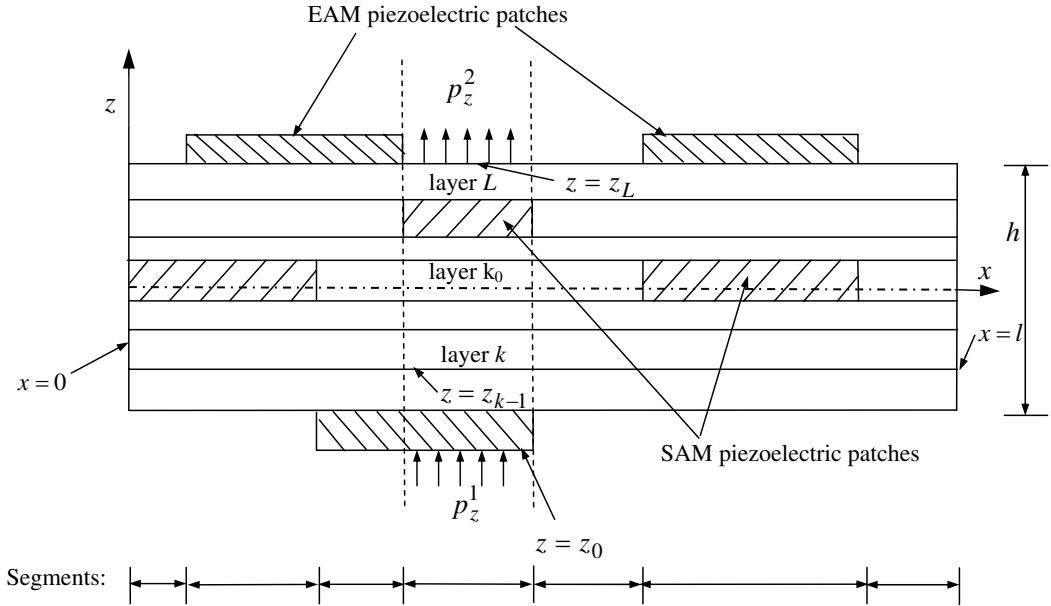

Figure 2. Geometry of hybrid beam with EAM and SAM piezoelectric patches.

may vary segment-wise. The z-coordinate of the bottom surface of the kth layer numbered from the bottom is denoted as z_{k-1} and its material axis x_1 has orientation angles α_k and β_k. The reference plane $z = 0$ either passes through or is the bottom surface of the k_0th layer. All the elastic and piezoelectric layers are perfectly bonded. The beam is loaded transversely on the bottom and top with no variation along the width b.

Two-dimensional coupled piezoelasticity solutions for piezoelectric beams/panels have revealed (see Section 6) that the electric potential ϕ follows a nearly quadratic distribution across the thickness for the extension mode [Dube et al. 1996] and a nearly cubic distribution with zero quadratic contribution for the shear mode [Parashar et al. 2005]. To model according to these observations, the potential field at time t is assumed as piecewise quadratic between n_ϕ points at $z = z_\phi^j$ across the thickness (Figure 3):

$$\phi(x, z, t) = \Psi_\phi^j(z)\phi^j(x, t) + \Psi_c^l(z)\phi_c^l(x, t), \tag{9}$$

where $\phi^j(x, t)$ is the electric potential at $z = z_\phi^j$, $\phi_c^l(x, t)$ denotes the quadratic component of electric potential at $z = (z_\phi^l + z_\phi^{l+1})/2$, and the summation convention is used with the indices j and l taking values $j = 1, 2, \ldots, n_\phi$ and $l = 1, 2, \ldots, n_\phi - 1$. $\Psi_\phi^j(z)$ and $\Psi_c^l(z)$ are the piecewise linear and quadratic functions, respectively, given by

$$\Psi_\phi^j(z) = \begin{cases} 0, & \text{if } z \leq z_\phi^{j-1} \quad \text{or} \quad z \geq z_\phi^{j+1}, \\ (z - z_\phi^{j-1})/(z_\phi^j - z_\phi^{j-1}), & \text{if } z_\phi^{j-1} < z < z_\phi^j, \\ (z_\phi^{j+1} - z)/(z_\phi^{j+1} - z_\phi^j), & \text{if } z_\phi^j < z < z_\phi^{j+1}, \end{cases}$$

$$\Psi_c^l(z) = \begin{cases} 4(z_\phi^{l+1} - z)(z - z_\phi^l)/(z_\phi^{l+1} - z_\phi^l)^2, & \text{if } z_\phi^l \leq z \leq z_\phi^{l+1}, \\ 0, & \text{otherwise.} \end{cases}$$

The surfaces of the piezoelectric sensor and actuator patches are always electroded with metallic coating, which makes the surfaces equipotential. Thus, ϕ^j should be taken as independent of x in a finite element
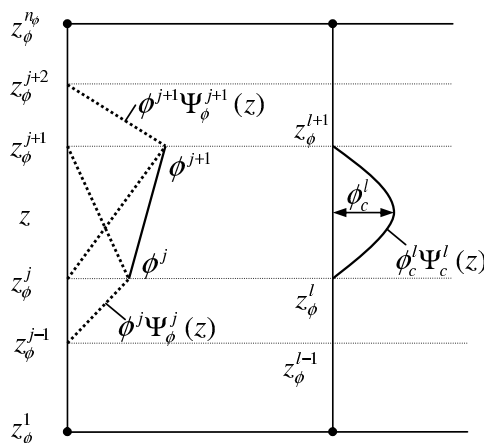

Figure 3. Approximation of ϕ along z-direction.

covering the electroded patch. With this description, ϕ in the piezoelectric layer can be modeled by a single layer discretization ($n_\phi = 2$) for the extension mode case and by a two-sublayer discretization ($n_\phi = 3$) for the shear mode case. In the latter case, since the quadratic contribution in the variation of ϕ is zero [Parashar et al. 2005], the mid-surface between the equipotential top and bottom surfaces will also be equipotential and, hence the above discretization holds well.

Exact 2D piezoelasticity solutions for hybrid beams and panels [Kapuria et al. 1997] have revealed that for moderately thick beams under electric field E_z the deflection w has significant variation across the thickness of the piezoelectric layers due to the significant contribution of E_z ($\bar{d}_{33}$ effect) to ε_z, which is much greater than the negligible contributions of the inplane electric field E_x and the stresses. Hence, w is approximated by integrating the constitutive Equation (4) for ε_z by neglecting the contributions of E_x and the stresses. It may be noted that the contribution of the inplane stresses to ε_z via Poisson's effect is neglected in most one-dimensional theories for elastic laminated beams, wherein w is approximated to be constant across the thickness. Thus, integrating $\varepsilon_z = w_{,z} = \bar{s}_{13}\sigma_x + \bar{s}_{23}\sigma_y + \bar{d}_{13}E_x + \bar{d}_{33}E_z \simeq -\bar{d}_{33}\phi_{,z}$ yields

$$w(x, z, t) = w_0(x, t) - \delta_1\left\{\bar{\Psi}_\phi^j(z)\phi^j(t) + \bar{\Psi}_c^l(z)\phi_c^l(t)\right\}, \tag{10}$$

where $\delta = 1$ or 0 depending upon whether or not the nonuniformity terms are considered, and

$$\bar{\Psi}_\phi^j(z) = \int_0^z \bar{d}_{33}\Psi_{\phi,z}^j(z)\,dz, \qquad \bar{\Psi}_c^l = \int_0^z \bar{d}_{33}\Psi_{c,z}^l(z)\,dz.$$

A subscript comma denotes differentiation. The axial displacement u is assumed to follow a global third-order variation with a layerwise linear variation across the thickness [Shu and Sun 1994; Kapuria et al. 2003]:

$$u(x, z, t) = u_k(x, t) - zw_{0,x}(x, t) + z\psi_k(x, t) + z^2\xi(x, t) + z^3\eta(x, t),$$

where u_k and ψ_k denote the translation and shear rotation variables of the kth layer, representing the layerwise linear variation, and ξ and η are the quadratic and cubic terms in z, representing the global cubic variation across the entire laminate thickness. The $2L + 3$ displacement variables u_k, ψ_k, ξ, η and w_0 are expressed in terms of only three variables by imposing the $2(L - 1)$ conditions of continuity of transverse shear stress τ_{zx} and u at the layer interfaces, and the two conditions of zero transverse shear at the top and bottom surfaces. This gives

$$u(x, z, t) = u_0(x, t) - zw_{0,x}(x, t) + R^k(z)\psi_0(x, t), \tag{11}$$

where u_0 denotes the axial displacement of the reference ($z = 0$) plane and ψ_0 is related to the shear strain of the reference plane. $R^k(z)$ is a layer-wise function of z for the kth layer given by

$$R^k(z) = \hat{R}_1^k + z\hat{R}_2^k + z^2\hat{R}_3 + z^3\hat{R}_4, \tag{12}$$

where the coefficients $\hat{R}_1^k$, $\hat{R}_2^k$, $\hat{R}_3$ and $\hat{R}_4$ are dependent on the lay-up and the material properties of the layers and are defined in the Appendix. Equation (11) for u can expressed as

$$u = f_1(z)\bar{u}_1, \tag{13}$$

where

$$\bar{u}_1 = \begin{bmatrix} u_0 & -w_{0,x} & \psi_0 \end{bmatrix}^{\mathrm{T}}, \qquad f_1(z) = \begin{bmatrix} 1 & z & R^k(z) \end{bmatrix}.$$

Using Equations (9), (10) and (13), the strains and the electric fields can be expressed as

$$
\begin{aligned}
\varepsilon_x &= u_{,x} = f_1(z)\bar{\varepsilon}_1, & E_x &= -\phi_{,x} = -f_3(z)\bar{\varepsilon}_3, \\
\gamma_{zx} &= u_{,z} + w_{,x} = f_2(z)\bar{\varepsilon}_2, & E_z &= -\phi_{,z} = -f_4(z)\bar{\varepsilon}_4,
\end{aligned}
\tag{14}
$$

with

$$
\begin{aligned}
\bar{\varepsilon}_1 &= \bar{u}_{1,x} = \begin{bmatrix} u_{0,x} & -w_{0,xx} & \psi_{0,x} \end{bmatrix}^{\mathrm{T}}, \quad \bar{\varepsilon}_2 = \begin{bmatrix} \psi_0 & -\phi_{c,x}^l \end{bmatrix}^{\mathrm{T}}, \quad \bar{\varepsilon}_3 = \phi_{c,x}^l, \quad \bar{\varepsilon}_4 = \begin{bmatrix} \phi_c^l & \phi^j \end{bmatrix}^{\mathrm{T}}, \\
f_2(z) &= \begin{bmatrix} R_{,z}^k(z) & \delta_1 \bar{\Psi}_c^l(z) \end{bmatrix}, \quad f_3(z) = \Psi_c^l(z), \quad f_4(z) = \begin{bmatrix} \Psi_{c,z}^l(z) & \Psi_{\phi,z}^j(z) \end{bmatrix}.
\end{aligned}
\tag{15}
$$

4. Variational principle for the coupled one-dimensional theory

Let p_z^1, p_z^2 be the normal forces per unit area on the bottom and top surfaces of the beam in direction z. Let there be distributed viscous resistance force with the distributed viscous damping coefficient c_1 per unit area per unit transverse velocity of the top surface of the beam. Using the notation

$$
\langle \ldots \rangle = \sum_{k=1}^{L} \int_{z_{k-1}^{+}}^{z_k^{-}} (\ldots) b \, dz
$$

for integration across the thickness, the extended Hamilton's principle [Tiersten 1969] for the beam reduces to

$$
\begin{aligned}
\int_x \Big[\langle \rho^k \ddot{u}\delta u + \rho^k \ddot{w}\delta w + \sigma_x \delta\varepsilon_x + \tau_{zx}\delta\gamma_{zx} - D_x\delta E_x - D_z\delta E_z \rangle - b p_z^1 \delta w(x, z_0, t) \\
- b\{ p_z^2 - c_1 \dot{w}(x, z_L, t) \}\delta w(x, z_L, t) + b D_z(x, z_0, t)\delta\phi^1 - b D_z(x, z_L, t)\delta\phi^{n\phi} \Big] dx \\
- \langle \sigma_x \delta u + \tau_{zx}\delta w + D_x\delta\phi \rangle \big|_x = 0, \quad (16)
\end{aligned}
$$

for all δu_0, δw_0, $\delta\psi_0$, $\delta\phi_c^l$, $\delta\phi^j$, where ρ^k is the material mass density of the kth layer. It has been observed elsewhere [Kapuria and Alam 2006] that the explicit contribution of electric potential terms in w (see Equation (10)) to inertia and damping can be neglected to achieve computational efficiency without sacrificing virtually any accuracy. Considering this, substituting the expressions (9), (10) and (13) for ϕ, w and u and (14) for ε_x, γ_{zx}, E_x, E_z into Equation (16) yields

$$
\begin{aligned}
\int_x \Big[\delta\bar{u}_1^{\mathrm{T}} I \ddot{\bar{u}}_1 + \delta w_0 \hat{I} \ddot{w}_0 + \delta\bar{\varepsilon}_1^{\mathrm{T}} F_1 + \delta\bar{\varepsilon}_2^{\mathrm{T}} F_2 + \delta\bar{\varepsilon}_3^{\mathrm{T}} F_3 + \delta\bar{\varepsilon}_4^{\mathrm{T}} F_4 - (P_2 + \hat{P}_2)\delta w_0 - P_\phi^j \delta\phi^j \Big] dx \\
- \Big[\bar{N}_x \delta\bar{u}_0 + \bar{V}_x \delta\bar{w}_0 - \bar{M}_x \delta\bar{w}_{0,x} + \bar{P}_x \delta\psi_0 + (\bar{H}^j - \delta_1 \bar{V}_\phi^j)\delta\bar{\phi}^j + (\bar{H}_c^l - \delta_1 \bar{V}_c^l)\delta\bar{\phi}_c^l \Big] \big|_x = 0, \quad (17)
\end{aligned}
$$

where an over-bar on the stress and electric resultants and on u_0, w_0, ψ_0, ϕ^j, ϕ_c^l means values at the ends. In this equation, I and $\hat{I}$ are the inertia terms defined by

$$
I = \langle \rho^k f_1^{\mathrm{T}}(z) f_1(z) \rangle = \begin{bmatrix} I_{11} & I_{12} & I_{13} \\ I_{12} & I_{22} & I_{23} \\ I_{13} & I_{23} & I_{33} \end{bmatrix}, \qquad \hat{I} = \langle \rho^k \rangle = I_{11}.
\tag{18}
$$

The stress resultants F_1 of σ_x, F_2, V_x, V_ϕ^j, V_c^l of τ_{zx}, and the electric displacement resultants F_3, H^j of D_x and F_4 of D_z are defined by

$$F_1 = \begin{bmatrix} N_x \\ M_x \\ P_x \end{bmatrix} = \langle f_1^{\mathrm{T}}(z)\sigma_x \rangle, \quad F_2 = \begin{bmatrix} Q_x \\ \bar{Q}_x^l \end{bmatrix} = \langle f_2^{\mathrm{T}}(z)\tau_{zx} \rangle, \quad F_3 = H_c^l = \langle f_3(z)D_x \rangle, \tag{19}$$

$$F_4 = \begin{bmatrix} G_c^l \\ G^j \end{bmatrix} = \langle f_4^{\mathrm{T}}(z)D_z \rangle, \quad H^j = \langle \Psi_\phi^j(z)D_x \rangle, \quad V_x = \langle \tau_{zx} \rangle, \quad V_\phi^j = \langle \bar{\Psi}_\phi^j(z)\tau_{zx} \rangle, \quad V_c^l = \langle \bar{\Psi}_c^l(z)\tau_{zx} \rangle. \tag{20}$$

The mechanical load P_2, electrical loads P_ϕ^j and damping load $\hat{P}_2$ are defined as

$$P_2 = b(p_z^1 + p_z^2), \qquad P_\phi^j = b\big[-p_z^1 \bar{\Psi}_\phi^j(z_0) - p_z^2 \bar{\Psi}_\phi^j(z_L) + D_{z_L}\delta_{jn_\phi} - D_{z_0}\delta_{j1} \big], \qquad \hat{P}_2 = -\hat{c}_1 \dot{w}_0,$$

where δ_{ij} is Kronecker's delta, $D_{z_0} = D_z(x, z_0, t)$, $D_{z_L} = D_z(x, z_L, t)$ and $\hat{c}_1 = bc_1$.

Define generalized strains $\bar{\varepsilon}$ and generalized stress resultants $\bar{F}$ as

$$\bar{\varepsilon} = \begin{bmatrix} \bar{\varepsilon}_1^{\mathrm{T}} & \bar{\varepsilon}_2^{\mathrm{T}} & \bar{\varepsilon}_3^{\mathrm{T}} & \bar{\varepsilon}_4^{\mathrm{T}} \end{bmatrix}^{\mathrm{T}}, \qquad \bar{F} = \begin{bmatrix} F_1^{\mathrm{T}} & F_2^{\mathrm{T}} & F_3^{\mathrm{T}} & F_4^{\mathrm{T}} \end{bmatrix}^{\mathrm{T}}. \tag{21}$$

Substituting the constitutive Equation (6) into Equation (19), the beam constitutive equation relating the generalized beam stress resultants $\bar{F}$ with the generalized strains $\bar{\varepsilon}$ can be obtained as

$$\bar{F} = \bar{D}\bar{\varepsilon}, \tag{22}$$

where

$$\bar{D} = \begin{bmatrix} A & 0 & e_1^{\mathrm{T}} & e_2^{\mathrm{T}} \\ 0 & \bar{A} & e_3^{\mathrm{T}} & e_4^{\mathrm{T}} \\ e_1 & e_3 & -\eta_1 & -\eta_2^{\mathrm{T}} \\ e_2 & e_4 & -\eta_2 & -\eta_3 \end{bmatrix}, \tag{23}$$

with

$$A = \langle \hat{Q}_{11} f_1^{\mathrm{T}}(z) f_1(z) \rangle = \begin{bmatrix} A_{11} & A_{12} & A_{13} \\ A_{12} & A_{22} & A_{23} \\ A_{13} & A_{32} & A_{33} \end{bmatrix}, \qquad \bar{A} = \langle \hat{Q}_{55} f_2^{\mathrm{T}}(z) f_2(z) \rangle = \begin{bmatrix} \bar{A}_{11} & \bar{A}_{12}^{l'} \\ \bar{A}_{12}^{l} & \bar{A}_{22}^{ll'} \end{bmatrix}_{n_\phi \times 3},$$

$$e_1 = \langle \hat{e}_{11} f_3^{\mathrm{T}}(z) f_1(z) \rangle = \begin{bmatrix} e_1^{1l} & e_2^{1l} & e_3^{1l} \end{bmatrix}_{(n_\phi-1)\times 3}, \qquad e_2 = \langle \hat{e}_{31} f_4^{\mathrm{T}}(z) f_1(z) \rangle = \begin{bmatrix} e_{11}^{2l} & e_{12}^{2l} & e_{13}^{2l} \\ e_{21}^{2j} & e_{22}^{2j} & e_{23}^{2j} \end{bmatrix}_{(2n_\phi-1)\times 3},$$

$$e_3 = \langle \hat{e}_{15} f_3^{\mathrm{T}}(z) f_2(z) \rangle = \begin{bmatrix} e_1^{3l} & \delta_1 e_2^{3ll'} \end{bmatrix}_{(n_\phi-1)\times n_\phi}, \qquad e_4 = \langle \hat{e}_{35} f_4^{\mathrm{T}}(z) f_2(z) \rangle = \begin{bmatrix} e_{11}^{4l} & \delta_1 e_{12}^{4ll'} \\ e_{21}^{4j} & \delta_1 e_{22}^{4jl'} \end{bmatrix}_{(2n_\phi-1)\times n_\phi},$$

$$\eta_1 = \langle \hat{\eta}_{11} f_3^{\mathrm{T}}(z) f_3(z) \rangle = \begin{bmatrix} \eta_1^{ll'} \end{bmatrix}_{(n_\phi-1)\times(n_\phi-1)}, \qquad \eta_2 = \langle \hat{\eta}_{13} f_4^{\mathrm{T}}(z) f_3(z) \rangle = \begin{bmatrix} \eta_1^{2ll'} \\ \eta_2^{2jl'} \end{bmatrix}_{(2n_\phi-1)\times(n_\phi-1)},$$

$$\eta_3 = \langle \hat{\eta}_{33} f_4^{\mathrm{T}}(z) f_4(z) \rangle = \begin{bmatrix} \eta_{11}^{3ll'} & \eta_{12}^{3lj'} \\ \eta_{12}^{3jl'} & \eta_{22}^{3jj'} \end{bmatrix}_{(2n_\phi-1)\times(2n_\phi-1)}. \tag{24}$$

The indices l' and j' take values $l' = 1, 2, \ldots, n_\phi - 1$ and $j' = 1, 2, \ldots, n_\phi$ like l and j, respectively. Using Equations (21) and (22), the contribution T^e of an element of length a to the integral in Equation (17) can be expressed as

$$T^e = \int_0^a \left[\delta \bar{u}^{\mathrm{T}} \bar{I} \ddot{\bar{u}} + \delta \bar{\varepsilon}^{\mathrm{T}} \bar{D} \bar{\varepsilon} - \delta \bar{u}^{\mathrm{T}} f_{u\phi} + \delta \bar{u}^{\mathrm{T}} \bar{C} \dot{\bar{u}} \right] dx, \tag{25}$$

where

$$\bar{u} = \begin{bmatrix} \bar{u}_1^{\mathrm{T}} & w_0 & \phi^j \end{bmatrix}^{\mathrm{T}} = \begin{bmatrix} u_0 & -w_{0,x} & \psi_0 & w_0 & \phi^j \end{bmatrix}^{\mathrm{T}}, \tag{26}$$

$$\bar{I} = \begin{bmatrix} I & 0 & 0 \\ 0 & \hat{I} & 0 \\ 0 & 0 & 0 \end{bmatrix}, \qquad \bar{C} = \begin{bmatrix} 0 & 0 & 0 \\ 0 & \hat{c}_1 & 0 \\ 0 & 0 & 0 \end{bmatrix}, \qquad f_{u\phi} = \begin{bmatrix} 0 & P_2 & P_\phi^j \end{bmatrix}^{\mathrm{T}}. \tag{27}$$

5. Finite element model

The highest derivatives of u_0, ψ_0, w_0, ϕ_c^l and ϕ^j appearing in the variational Equation (17) are $u_{0,x}$, $w_{0,xx}$, $\psi_{0,x}$, $\phi_{c,x}^l$ and ϕ^j. Accordingly, to meet the convergence requirement, the interpolation functions for u_0, $w_{0,x}$, ψ_0 and ϕ_c^l must be continuous at the element boundaries. These variables are interpolated using two physical nodes as shown in Figure 4. The variable w_0 is interpolated using the C^1-continuous cubic Hermitian function in terms of the nodal values of w_0, $w_{0,x}$, and u_0, ψ_0, ϕ_c^l are interpolated using a C^0-continuous linear Lagrangian function. Since ψ_0 is a measure of shear strain at the reference plane and not the rotation of the normal, a linear interpolation for ψ_0 does not cause shear locking [Kapuria and Alam 2006]. Thus, at the element level, each physical node will have four degrees of freedom, u_0, w_0, $w_{0,x}$, ψ_0, for the displacements and $(n_\phi - 1)$ degrees of freedom of ϕ_c^l for the electric potential.

As stated in Section 3, ϕ^j is constant in an element. However, if a number of elements fall in the same electroded surface, it would be necessary to impose the constraint of equality on the electric DOF ϕ^j of the elements on the same electroded surface. To avoid this task, the set of ϕ^j of the equipotential surfaces of piezoelectric patches in a beam section are associated with a separate *electric node* p, see Figure 4, which can be connected to several elements. The electric node does not have any x-coordinate unlike the physical nodes, and has n_ϕ degrees of freedom. This concept not only eliminates the need of imposing equality constraints on the electric DOF for equipotential condition, but also results in
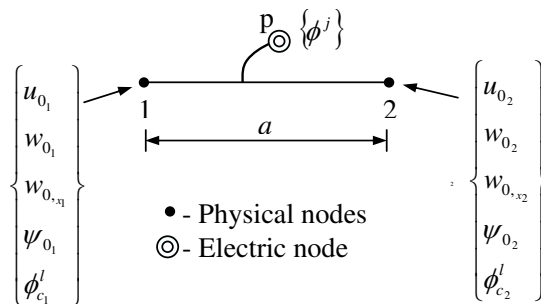

Figure 4. Degrees of freedom for the beam element.

significant reduction in the number electric DOF. Thus, denoting the values of an entity $(\,.\,)$ at the physical node i by $(\,.\,)_i$, the variables $u_0, \psi_0, w_0, \phi_c^l$ are interpolated in an element of length a as

$$u_0 = N u_0^e, \qquad w_0 = \bar{N} w_0^e, \qquad \psi_0 = N \psi_0^e, \qquad \phi_c^l = N \phi_c^{le}, \tag{28}$$

with

$$u_0^e = \begin{bmatrix} u_{0_1} & u_{0_2} \end{bmatrix}^{\mathrm{T}}, \quad w_0^e = \begin{bmatrix} w_{0_1} & w_{0,x_1} & w_{0_2} & w_{0,x_2} \end{bmatrix}^{\mathrm{T}}, \quad \psi_0^e = \begin{bmatrix} \psi_{0_1} & \psi_{0_2} \end{bmatrix}^{\mathrm{T}}, \quad \phi_c^{le} = \begin{bmatrix} \phi_{c_1}^l & \phi_{c_2}^l \end{bmatrix}^{\mathrm{T}},$$

$$N = \begin{bmatrix} N_1 & N_2 \end{bmatrix}, \qquad \bar{N} = \begin{bmatrix} \bar{N}_1 & \bar{N}_2 & \bar{N}_3 & \bar{N}_4 \end{bmatrix}, \qquad N_1 = 1 - (x/a), \qquad N_2 = \frac{x}{a},$$

$$\bar{N}_1 = 1 - \frac{3x^2}{a^2} + \frac{2x^3}{a^3}, \qquad \bar{N}_2 = x - \frac{2x^2}{a} + \frac{x^3}{a^2}, \qquad \bar{N}_3 = \frac{3x^2}{a^2} - \frac{2x^3}{a^3}, \qquad \bar{N}_4 = -\frac{x^2}{a} + \frac{x^3}{a^2}.$$

Defining the element generalized displacement vector U^e as $U^{e\mathrm{T}} = [u_0^{e\mathrm{T}} \ w_0^{e\mathrm{T}} \ \psi_0^{e\mathrm{T}} \ \phi_c^{le\,\mathrm{T}} \ \phi^j]$ and using Equation (28), the generalized displacements $\bar{u}$ and strains $\bar{\varepsilon}$ defined in Equations (15), (21) and (26) can be related to U^e as

$$\bar{u} = \hat{N} U^e, \qquad \bar{\varepsilon} = \hat{B} U^e, \tag{29}$$

where

$$\hat{N} = \begin{bmatrix} N & 0 & 0 & 0 & 0 \\ 0 & -\bar{N}_{,x} & 0 & 0 & 0 \\ 0 & 0 & N & 0 & 0 \\ 0 & \bar{N} & 0 & 0 & 0 \\ 0 & 0 & 0 & 0 & 1 \end{bmatrix}, \qquad \hat{B} = \begin{bmatrix} N_{,x} & 0 & 0 & 0 & 0 \\ 0 & -\bar{N}_{,xx} & 0 & 0 & 0 \\ 0 & 0 & N_{,x} & 0 & 0 \\ 0 & 0 & N & 0 & 0 \\ 0 & 0 & 0 & -N_{,x} & 0 \\ 0 & 0 & 0 & N_{,x} & 0 \\ 0 & 0 & 0 & N & 0 \\ 0 & 0 & 0 & 0 & 1 \end{bmatrix}. \tag{30}$$

Substituting the expressions for $\hat{u}$ and $\hat{\varepsilon}$ from Equation (29) into Equation (25), T^e can be expressed as

$$T^e = \int_0^a \delta U^{e\mathrm{T}} \big[\hat{N}^{\mathrm{T}} \bar{I} \hat{N} \ddot{U}^e + \hat{N}^{\mathrm{T}} \bar{C} \hat{N} \dot{U}^e + \hat{B}^{\mathrm{T}} \bar{D} \hat{B} U^e - \hat{N}^{\mathrm{T}} f_{u\phi} \big] \, dx$$

$$= \delta U^{e\mathrm{T}} \big[M^e \ddot{U}^e + C^e \dot{U}^e + K^e U^e - P^e \big],$$

where M^e, C^e and K^e are the generalized element inertia, damping and stiffness matrices, and P^e is the element load vector defined as

$$M^e = \int_0^a \hat{N}^{\mathrm{T}} \bar{I} \hat{N} \, dx = \begin{bmatrix} M_{uu}^e & 0 & 0 \\ 0 & 0 & 0 \\ 0 & 0 & 0 \end{bmatrix}, \qquad C^e = \int_0^a \hat{N}^{\mathrm{T}} \bar{C} \hat{N} \, dx = \begin{bmatrix} C_{uu}^e & 0 & 0 \\ 0 & 0 & 0 \\ 0 & 0 & 0 \end{bmatrix},$$

$$K^e = \int_0^a \hat{B}^{\mathrm{T}} \bar{D} \hat{B} \, dx = \begin{bmatrix} K_{uu}^e & K_{ul}^e & K_{uj}^e \\ K_{lu}^e & K_{ll}^e & K_{lj}^e \\ K_{ju}^e & K_{jl}^e & K_{jj}^e \end{bmatrix}, \qquad P^e = \int_0^a \hat{N}^{\mathrm{T}} f_{u\phi} \, dx = \begin{bmatrix} P_u^e \\ 0 \\ P_j^e \end{bmatrix}. \tag{31}$$

The subscripts u, l and j correspond to the mechanical displacement variables, ϕ_c^l and ϕ^j, respectively. The elements of the submatrices in Equation (31) are listed in the Appendix. The elements of the same

electroded surface are connected to one electric node having a global degree of freedom number for the potential ϕ^j of the equipotential surface at $z = z_\phi^j$. The node numbers of the two physical nodes and the electric node of each element are stored in the element connectivity matrix. The element matrices are then assembled using the standard assembly procedure, by storing the global DOF numbers of all element DOF in an index matrix, and placing the elements of the element matrix in the appropriate locations of the global matrix, according to the global DOF numbers [Chandrupatla and Belegundu 2002]. Summing up contributions of all elements to the integral in Equation (17), the system equation can be obtained as

$$M\ddot{U} + C\dot{U} + KU = P, \tag{32}$$

in which M, C, K are assembled from the element matrices M^e, C^e, K^e and U, P are the assembled counterparts of U^e, P^e.

At the actuated surfaces (closed circuit condition), electric potentials have known prescribed values. At the sensory surfaces under open circuit condition, the electric loads are known (zero electric charge, that is, $\int_0^{a_e} b D_z\, dx = 0$, a_e being the length of the electrode), but the electric potentials are unknown. The system vector U is partitioned into vectors of mechanical displacements $\bar{U}$, unknown output voltages Φ_s and known input actuation voltages Φ_a. Thus, Equation (32) can be partitioned and arranged as

$$\begin{bmatrix} M^{uu} & 0 & 0 \\ 0 & 0 & 0 \\ 0 & 0 & 0 \end{bmatrix} \begin{bmatrix} \ddot{\bar{U}} \\ \ddot{\Phi}_s \\ \ddot{\Phi}_a \end{bmatrix} + \begin{bmatrix} C^{uu} & 0 & 0 \\ 0 & 0 & 0 \\ 0 & 0 & 0 \end{bmatrix} \begin{bmatrix} \dot{\bar{U}} \\ \dot{\Phi}_s \\ \dot{\Phi}_a \end{bmatrix} + \begin{bmatrix} K^{uu} & K^{us} & K^{ua} \\ K^{su} & K^{ss} & K^{sa} \\ K^{au} & K^{as} & K^{aa} \end{bmatrix} \begin{bmatrix} \bar{U} \\ \Phi_s \\ \Phi_a \end{bmatrix} = \begin{bmatrix} \bar{P} \\ Q_s \\ Q_a \end{bmatrix}. \tag{33}$$

Equation (33) yields the output potentials as

$$\Phi_s = -(K^{ss})^{-1}\big[K^{su}\bar{U} + K^{sa}\Phi_a - Q_s\big]. \tag{34}$$

Substitution of Equation (34) into Equation (33) yields

$$M^{uu}\ddot{\bar{U}} + C^{uu}\dot{\bar{U}} + \big[K^{uu} - K^{us}(K^{ss})^{-1}K^{su}\big]\bar{U} = \bar{P} - K^{us}(K^{ss})^{-1}Q_s - \big[K^{ua} - K^{us}(K^{ss})^{-1}K^{sa}\big]\Phi_a. \tag{35}$$

For undamped free vibration, the damping matrix C^{uu} and the right-hand side vector of the above equation are set to zero. The resulting generalized eigenvalue problem is solved using subspace iteration method [Petyt 1990] to obtain the undamped natural frequencies ω and the mode shapes. For transient response, Equation (35) can be solved using Newmark direct time integration method [Petyt 1990]. The advantage of first partitioning the electric potential vector Φ into Φ_s and Φ_a, and then carrying out the condensation as per Equations (34) and (35) is that it can model the response of the structure under any electric boundary conditions, namely, in the active mode (closed circuit), the sensory mode (open circuit) and the combined *active-sensory* mode (some electrodes in open circuit and some in closed circuit). In contrast, if the entire electric potential vector Φ is condensed out as in [Tzou and Tseng 1990], the resulting free vibration problem would give only the open circuit frequencies.

Equation (17) indicates that the mechanical boundary conditions for simply-supported, clamped and free ends are:

simply-supported	$N_x = 0,$	$w_0 = 0,$	$M_x = 0,$	$P_x = 0,$
clamped	$u_0 = 0,$	$w_0 = 0,$	$w_{0,x} = 0,$	$\psi_0 = 0,$
free	$N_x = 0,$	$V_x = 0,$	$M_x = 0,$	$P_x = 0.$

6. Results and discussion

6.1. *Validation.* In order to validate the new FE formulation and the computer program developed, cantilever plane strain beams (a) and (b) made of aluminum substrate with surface-bonded and embedded PZT-5H layers, respectively, are considered, which have been analyzed in [Zhang and Sun 1996; Benjeddou et al. 1999]. The configurations and the dimensions of the beams are shown in Figure 5 and the material properties are selected as in the references mentioned above:

(i) PZT-5H:

$$\{c_{11}, c_{22}, c_{33}, c_{12}, c_{23}, c_{31}, c_{44}, c_{55}, c_{66}\} = \{126, 126, 117, 79.5, 84.1, 84.1, 23, 23, 23.25\} \text{ GPa},$$

$$\{e_{31}, e_{32}, e_{33}, e_{15}, e_{24}\} = \{-6.5, -6.5, 23.3, 17.0, 17.0\} \text{ C/m}^2,$$
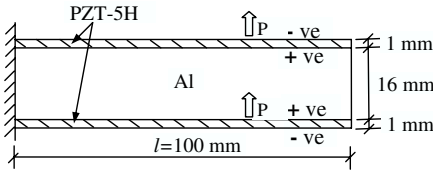
$$\{\eta_{11}, \eta_{22}, \eta_{33}\} = \{1.503, 1.503, 1.3\} \times 10^{-8} \text{ F/m}, \rho = 7500 \text{ kg/m}^3;$$
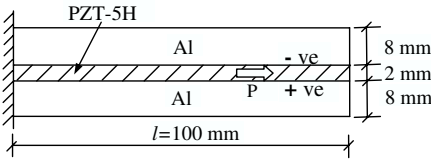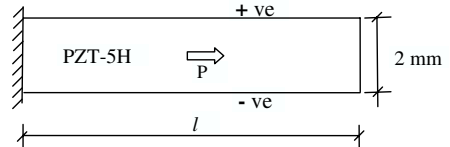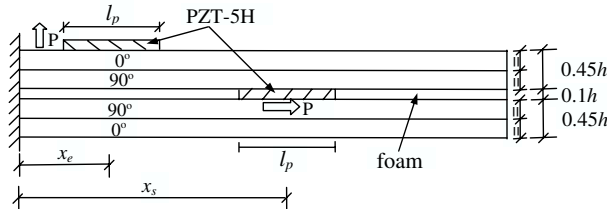

Adaptive SAM beam (a)
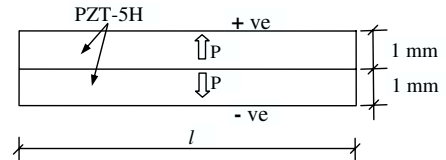
Bimorph EAM beam (c)

Adaptive EAM beam (b)

SAM piezoelecric beam (d)

Adaptive SAM-EAM composite beam (e)

Figure 5. Configurations of SAM and EAM beams.

(ii) Al:

$$Y_1 = Y_2 = Y_3 = Y = 70.3\,\text{GPa},\ \nu_{12} = \nu_{23} = \nu_{31} = \nu = 0.345,\ \rho = 2710\,\text{kg/m}^3,$$

where Y_i and ν_{ij} denote the Young's moduli and Poisson's ratios.

In beam (a) the piezoelectric layer embedded between the two aluminum layers is polarized along the axial direction x ($\alpha = 0$, $\beta = -90°$), and hence an applied electric potential across its thickness gives rise to shear mode actuation. For actuation, a voltage of 20 V is applied at the bottom surface of the actuator, while its top surface is grounded. In beam (b) the surface-mounted PZT layers at the top and bottom of the aluminum substrate are polarized along the thickness direction z, and hence an applied electric potential across its thickness causes extension mode actuation. In this case a potential of -10 V is applied at the top and bottom surfaces of the beam for actuation. Both the beams are modeled with 20 equal-size elements to obtain converged results. The shear mode piezoelectric layer in beam (a) is divided into two sublayers and those in beam (b) are modeled as one sublayer for the discretization of potential ϕ. The present results for the deflection profile of the centerline ($z = 0$) are compared in Figure 6 with the FE FSDT results of Benjeddou et al. [1999] for beam (a) and with the analytical FSDT solution of Zhang and Sun [1996] for beam (b). It is found that the present results are in excellent agreement with the reference results in both cases. The beams are also analyzed using the commercial FE software ABAQUS employing eight-node plane strain element, CPE8RE, with a mesh of 20 (thickness)×50 (length). The 2D FE results are also plotted in Figure 6, which compare very well with the present results.

The present result for the tip deflection of the shear actuated beam (a) is compared in Table 1 with other available results. While the present result and those obtained using a sandwich model using FSDT for the core [Zhang and Sun 1996; Benjeddou et al. 1999] match closely with the 2D FE results of ABAQUS, while those reported by Trindade and Benjeddou [2005] considering an improved sandwich model with the core modeled with the TOT have considerable difference from the 2D results. This difference between the FSDT and the TOT modeling of the core predicted by Trindade and Benjeddou [2005] appears to be inconsistent, since the 2D FE solution does not involve any approximation on the through-the-thickness variations of field variables and hence are accurate. The electric field E_z in the
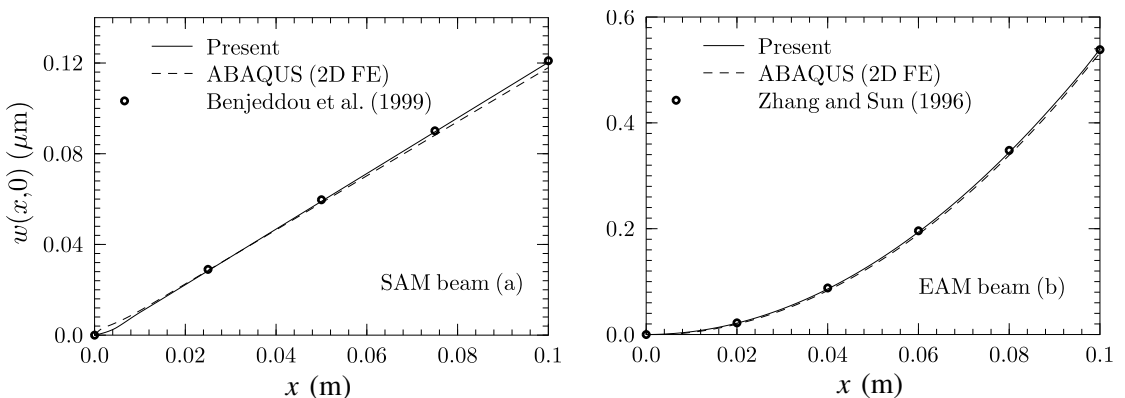

Figure 6. Central deflection of beams with shear and extension mode actuators under potential load.

Model	$w(l, 0)$ (μm)	E_z (V/mm)
Present	0.1203	10
FSDT analytic [Zhang and Sun 1996]	0.1196	10
FSDT FE [Benjeddou et al. 1999]	0.1196	10
TSDT FE, ϕ linear [Trindade and Benjeddou 2005]	0.0999	–
TSDT FE, ϕ cubic [Trindade and Benjeddou 2005]	0.0879	6.94–16.11
ABAQUS	0.1180	10

Table 1. Tip deflection of SAM beam (a) under actuation potential of 20 V.

piezoelectric layer obtained from different models are also compared in Table 1. It is seen from the 2D FE results that E_z is almost uniform across the thickness of the PZT layer and the same is predicted by the present model. Trindade and Benjeddou [2005] have, however, reported a quadratic variation of E_z across the thickness, which is attributed to the induced potential due to the direct piezoelectric effect. This also seems incorrect, since the 2D results show no such trend. It may also be noted that while Zhang and Sun [1996] and Benjeddou et al. [1999] have assumed a linear variation for the electric potential ϕ, the present model with 2 sublayers in the PZT layer can capture the cubic variation of ϕ, and has still predicted a practically linear variation of ϕ as in the 2D solution. The cubic component of ϕ induced to the direct piezoelectric effect is predicted as 0.010 V only, which is very small compared to the applied electric potential of 20 V.

Beams (a) and (b) are also analyzed for a uniform pressure load of $p_z^2 = 1000$ N/m² with the surfaces of the PZT layers kept at zero potential (closed circuit condition). The midsurface deflection obtained from the present one-dimensional model is compared with 2D FE result of ABAQUS in Figure 7. The two results are found to be in excellent agreement for both SAM and EAM beams.

No results for the free vibration response of the above beams have been reported in literature. To validate the present model for the free vibration response, the present results for natural frequencies of the first 7 modes (of which five are flexural modes and two are extension modes) are compared in Table 2
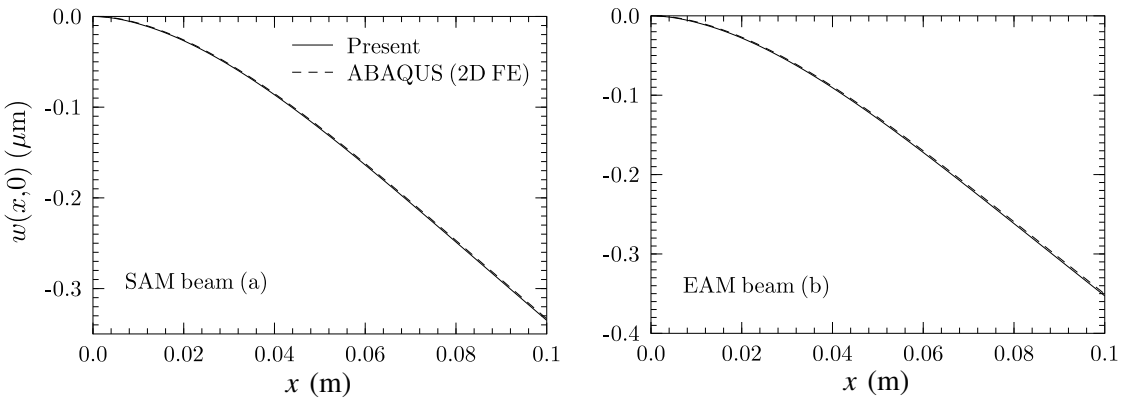

Figure 7. Central deflection of beams with shear and extension mode actuators under pressure load.

Beam	Mode, n	Type	ABAQUS (2D FE)	Present model (# of elts.) 10	20	30
				Frequency, f_n (Hz)		
(a)	1	flexural	1414.6	1404.2	1403.6	1403.4
	2	flexural	7796.2	7728.6	7693.5	7684.0
	3	extension	12799	12251	12242	12240
	4	flexural	18876	18757	18582	18537
	5	flexural	31767	31693	31234	31125
	6	extension	38057	37056	36801	36754
	7	flexural	45598	45764	44815	44622
(b)	1	flexural	1370.8	1365.1	1364.5	1364.4
	2	flexural	7475.6	7471.5	7439.6	7430.9
	3	extension	12345	12292	12282	12280
	4	flexural	17996	18053	17897	17855
	5	flexural	30172	30381	29969	29868
	6	extension	36752	37179	36922	36875
	7	flexural	43207	43715	42870	42691

Table 2. Closed circuit natural frequencies of SAM beam (a) and EAM beam (b).

with the 2D FE results obtained using ABAQUS. The present results are obtained with 10, 20 and 30 equal-size elements to study the convergence. It is observed that very good convergence is achieved with 20 elements, and the present results are in excellent agreement with the 2D FE results with a maximum error of 0.8% for the fundamental frequency and 2% for the higher mode frequencies up to the 7th mode (5th flexural mode).

6.2. Bimorph EAM beam. A simply-supported plane-stress (thin width) bimorph extension mode actuator beam (c) made of two layers of PZT-5H polarized along opposite transverse directions, see Figure 5, is analyzed for the following two load cases:

(1) Uniform potential $\phi^{n_\phi} = \phi_0$ applied on the top surface with the bottom being grounded ($\phi^1 = 0$).

(2) Uniform pressure $p_z^2 = -p_0$ applied on the top surface with $\phi^{n_\phi} = \phi^1 = 0$ (closed circuit condition).

These results and all subsequent ones for beams (c) and (d) for the potential and pressure load cases are nondimensionalized as:

1. $\bar{w} = 10w/S^2 d_0 \phi_0,$ $\bar{\sigma}_x = \sigma_x h/10Y_0 d_0 \phi_0,$ $\bar{\phi} = \phi/\phi_0,$

2. $\bar{w} = wY_0/lS^3 p_0,$ $\bar{\sigma}_x = \sigma_x/S^2 p_0,$ $\bar{\phi} = 100\phi Y_0 d_0/hS^2 p_0,$

with $Y_0 = 60$ GPa and $d_0 = 274.8 \times 10^{-12}$ CN^{-1}. S is the span-to-thickness ratio (l/h). Using symmetry the half length of the beam is discretized with 20 equal-size elements and only one electric node is used to model the closed circuit equipotential surfaces at the top and bottom. Each PZT layer is considered as
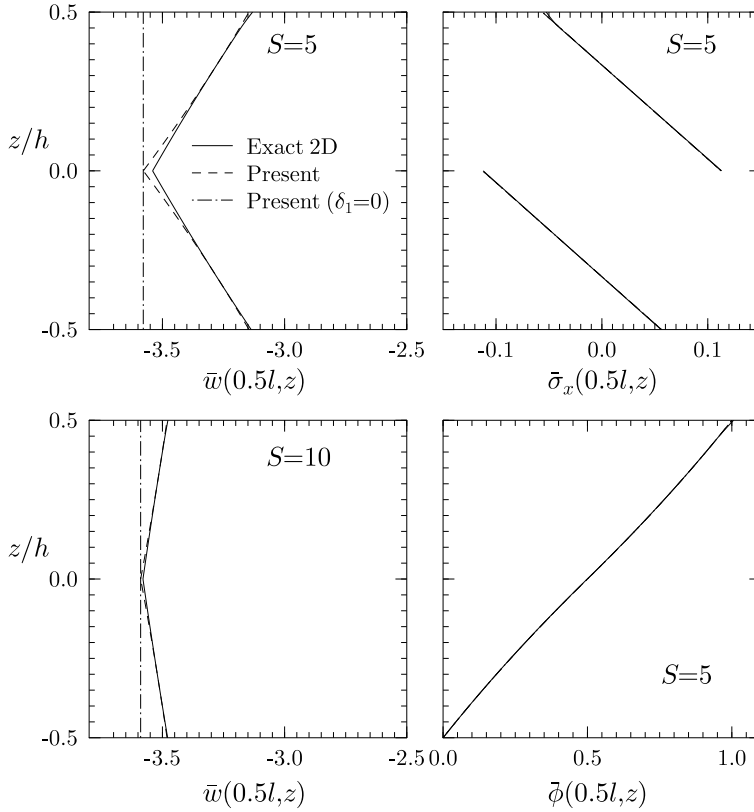
Figure 8. Through-the-thickness distributions of $\bar{w}, \bar{\sigma}_x, \bar{\phi}$ for bimorph EAM beam (c) under potential load 1.

one sublayer for ϕ-discretization. It is pertinent to note here that the number of electric potential DOF for the piezoelectric surfaces is only 3 in the present model using the electric node, which would have been 63 if the traditional concept of nodal electric variables were used. For a 2D plate or shell problem this reduction will be even more significant.

The present through-the-thickness distributions of deflection $\bar{w}$, axial stress $\bar{\sigma}_x$ and potential $\bar{\phi}$ are compared in Figure 8 with the exact 2D solution of Kapuria et al. [1997] for the potential load of case (1). In order to illustrate the effect of exclusion of the layerwise term in w in Equation (10), the present results with $\delta_1 = 0$ are also presented in Figure 8. It is observed that under the potential load, the top and bottom layers of the bimorph actuator undergo, respectively, expansion and contraction of their thickness, and the resulting variation of w across the thickness is accurately predicted by the present model with $\delta_1 = 1$. As expected, the model with $\delta_1 = 0$ is unable to predict this variation. The nonuniform variation of w is more significant for the thick beam with $S = 5$ than the thinner one with $S = 10$. The present results for the variations of $\bar{\sigma}_x$ and $\bar{\phi}$ are indistinguishable from the 2D results. The deflection profile of the centerline and the through-the-thickness distributions of $\bar{\sigma}_x$ and $\bar{\phi}$ for the beam (c) under pressure load case (2) are presented in Figure 9. The results are in excellent agreement with the exact 2D results. The present model is able to accurately predict the quadratic variation of ϕ induced due to the direct piezoelectric
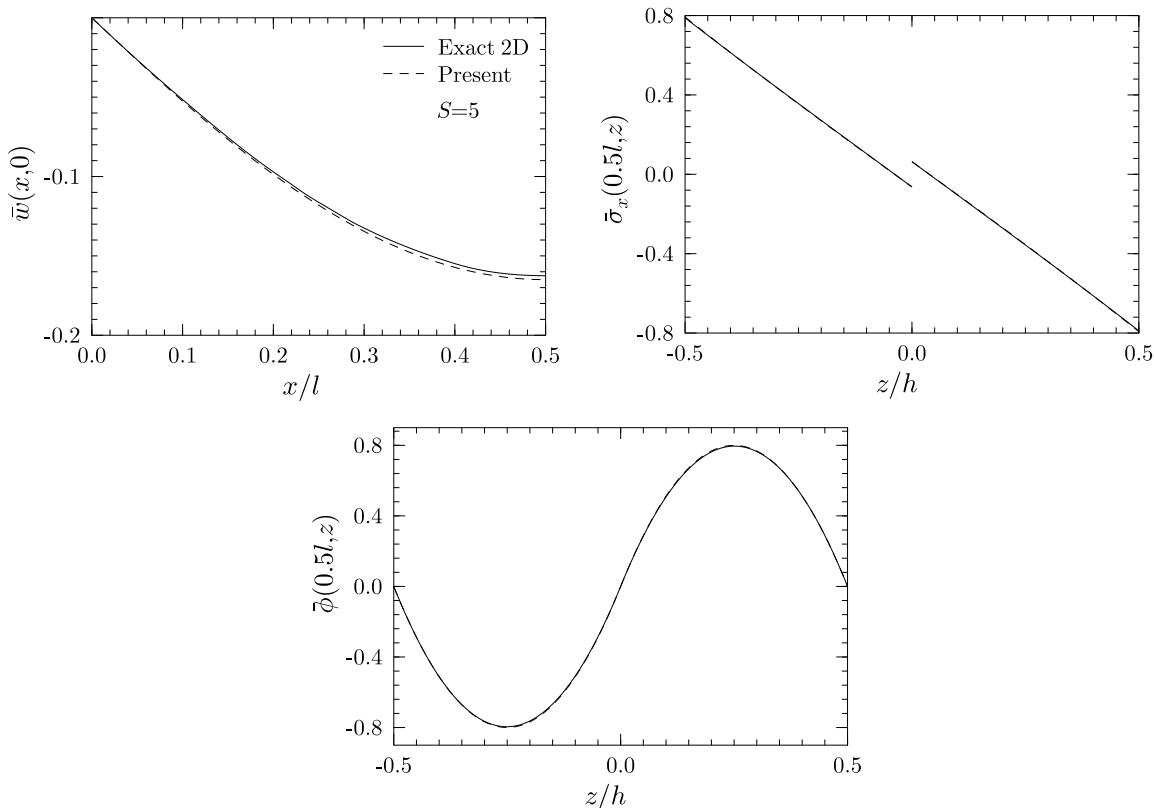
Figure 9. Deflection profile and distributions of $\bar{\sigma}_x$ and $\bar{\phi}$ for bimorph EAM beam (c) under pressure load 2.

effect across the thickness. In earlier publications of Kapuria et al. [2003] it has been observed that, with a sublayerwise linear approximation for the electric potential, a piezoelectric layer needs to be divided into 4 sublayers to capture the quadratic variation of the induced potential accurately, and also to achieve convergence in results. Thus, the number of electric variables with such an approximation would be 189 ($= 9 \times 21$), which is reduced to 45 ($= 2 \times 21 + 3$) in the present model.

6.3. *Shear mode pointer.* A cantilever plane-stress shear mode pointer beam (d), see Figure 5, of PZT-5H with span-to-thickness ratio $S = 10$ is analyzed for an uniform pressure load of case (2), using the

Entity	2D FE	Present model	
		$n_\phi = 3$	$n_\phi = 2$
$\bar{w}(l, 0)$	-1.839	-1.833	-1.884
$\bar{\phi}(0, z)\|_{\max}$	11.048	11.927	0.0
$\bar{\sigma}_x(0, 0.5h)$	2.772	2.618	3.049

Table 3. Effect of ϕ-discretization in shear pointer beam (d) under pressure load ($S = 10$).
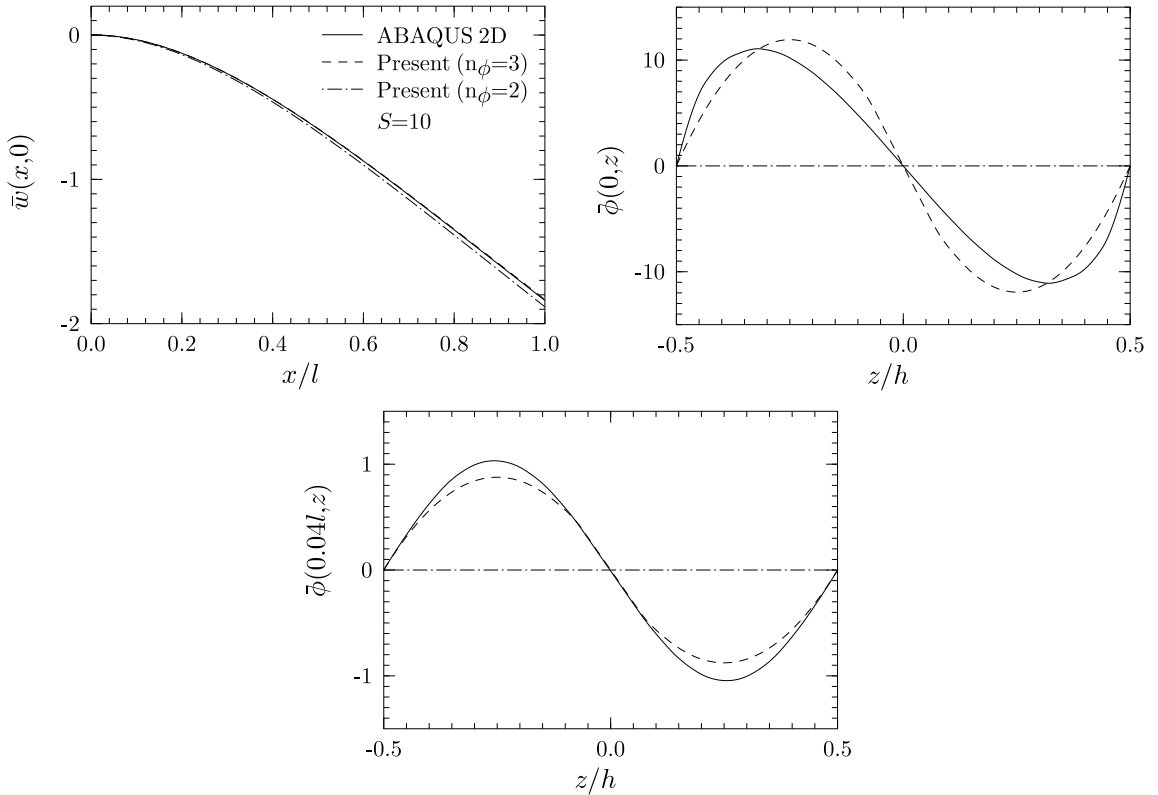
Figure 10. Deflection profile and distribution of $\bar{\phi}$ for shear pointer beam (d) under pressure load 2.

present model and the 2D FE model with eight-node plane stress element, CPS8RE, in ABAQUS. For the present model results are obtained considering 1 ($n_\phi = 2$) and 2 ($n_\phi = 3$) sublayers in the single-layer beam for discretization of ϕ across the thickness. For the 2D FE model the beam is modeled with 1600 [100 (length) $\times$ 16 (thickness)] elements to obtain converged results. The deflection profile of the centerline and the distributions of ϕ across the thickness at two locations at and near the clamped end are plotted in Figure 10. The tip deflection and the maximum values of $\bar{\sigma}_x$ and $\bar{\phi}$ are listed in Table 3. It is revealed from the 2D FE results that the electric potential induced in the shear actuator due to direct piezoelectric effect follows a cubic variation across the thickness, which is quite accurately predicted by the present model with $n_\phi = 3$. It is also revealed that the quadratic component in the third-order variation of ϕ is zero yielding zero potential at the midsurface. This fact justifies the use of two sublayers having quadratic variation of ϕ across each sublayer and an equipotential surface at the midsurface to model the cubic distribution of ϕ. With one sublayer ($n_\phi = 2$), however, the estimated induced potential is zero as expected. Consequently, the deflection profile predicted by the present model with $n_\phi = 3$ matches closely with the 2D FE results, whereas that with one sublayer ($n_\phi = 2$) is not as accurate. It can be seen from Table 3 that $\bar{\sigma}_x$ predicted with $n_\phi = 2$ is also less accurate than that with $n_\phi = 3$. The variation ϕ across the thickness of the beam under the same pressure load, but with the top surface having 5 electrode segments under open circuit condition, is shown in Figure 11 for two locations, $x = 0, l/2$. The
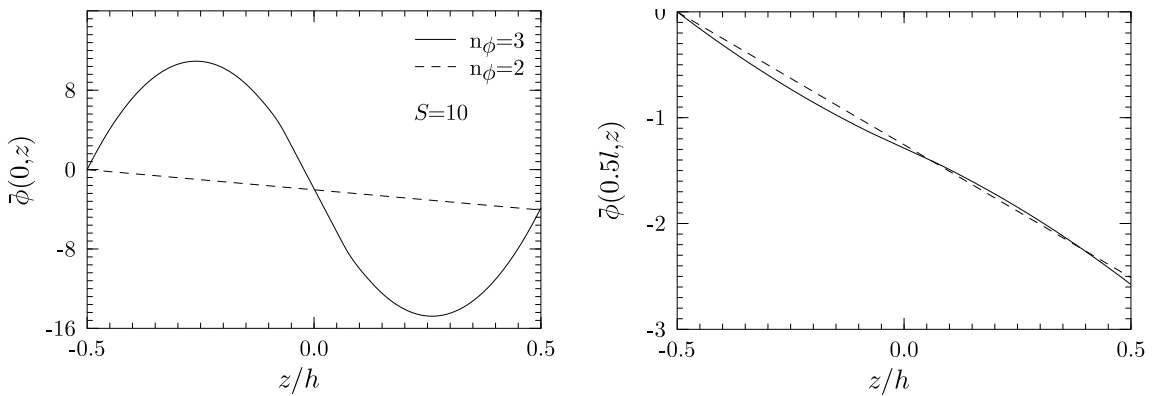
Figure 11. Distribution of $\bar{\phi}$ for shear pointer beam (d) under pressure load with open circuit condition at top.

distribution is again cubic, the cubic component being larger than the linear component at the clamped end. However, at the midspan the cubic component is much smaller than the linear one. It has been observed that the distribution becomes almost linear near the free end. With $n_\phi = 2$, even though the cubic variation is completely missed, the open circuit potential at the top surface is accurately predicted at $x = 0$. However, it is not as accurately predicted at $x = l/2$.

6.4. *Extension and shear mode sensors.* The sensory response of an extension mode bimorph beam (c) and a shear mode beam (d), both under cantilever boundary condition, is obtained for (i) an uniform pressure load (UDL) p_0 on the top and (ii) a concentrated load $P = p_0 l/2$ at the free end (tip load) for thickness ratio $S = 10$. The top surface is in open circuit condition while the bottom surface is grounded. Both beams are modeled with 20 equal-size elements. In order to illustrate the effect of segmentation of the electroded sensor surface, results are obtained with the beam surfaces divided into 1, 2, 5, 10 and 20 electroded patches. This is modeled by assigning an electric node to each electroded patch pair. The variation of the sensory potential induced at the top surface for the two load cases is plotted in Figures 12
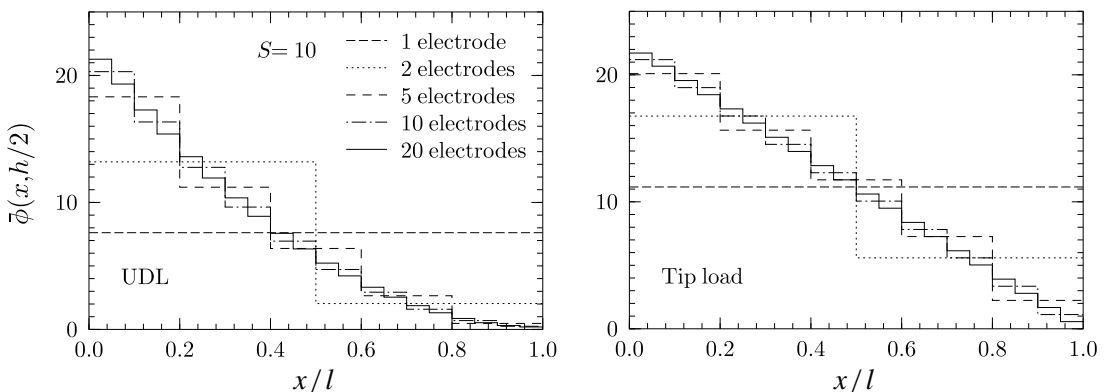

Figure 12. Sensory potential for varying number of electrodes for cantilever EAM beam (c).
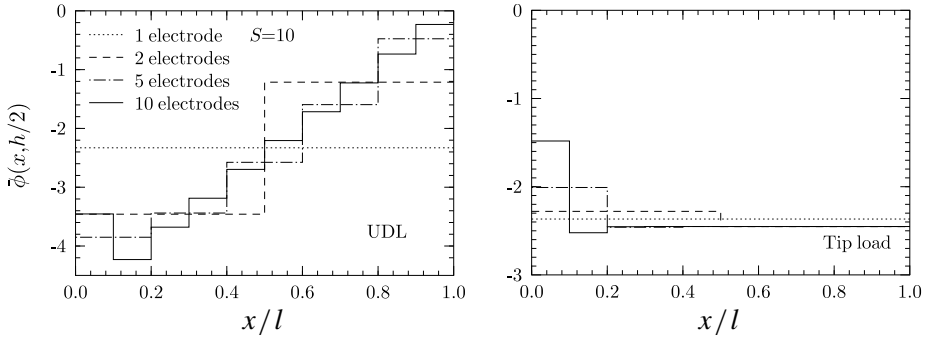
Figure 13. Sensory potential for varying number of electrodes for cantilever SAM beam (d).

and 13, respectively. It is observed that for the extension mode sensor (c), the sensory potential of the electrodes follows a step-wise quadratic variation for the UDL and a step-wise linear variation for the tip load, since it is related to the induced bending moment (axial stress). For the shear mode sensor (d), however, the sensory potential of the electrodes follows a stepwise linear variation for the UDL and an uniform variation for the tip load (except near the clamped end, which is believed to be due to boundary effect). This is because the sensory potential in shear mode is proportional to the induced shear. Thus, the sensory potential is independent of the electrode location, as long as the applied load causes constant transverse shear (as for tip load), but varies with the electrode location if the transverse shear changes (as for the UDL).

It is apparent from Figures 12 and 13 that the potential induced in a larger electrode is approximately equal to the area average of the potentials induced when it is divided into smaller segments. The tip deflection w and the maximum sensory potential ϕ induced for varying number of electrodes are presented in Tables 4 and 5 for beams (c) and (d), respectively. For comparison, the deflection for the closed circuit condition of the top surface (with zero potential) is also listed in these tables. It is revealed that the tip deflections of beam (c) with 1 and 20 electrodes differ by 4% and 3% for the UDL and the tip load, respectively. For the shear mode beam (d), however, the tip deflection is independent of the number of electrodes. It is also observed that, for the extension mode beam, the closed circuit deflection differs from the open circuit deflection with 20 electrodes by about 12.5% for both the load cases. For the shear

Load case	Entity	Number of electrodes					Closed circuit
		1	2	5	10	20	
UDL	$\bar{w}(l,0)$	-1.3422	-1.3021	-1.2910	-1.2894	-1.2890	-1.4516
	$\bar{\phi}(0.5h)|_{\max}$	7.6158	13.195	18.315	20.297	21.277	0
Tip load	$\bar{w}(l,0)$	-1.7703	-1.7302	-1.7192	-1.7174	-1.7170	-1.9308
	$\bar{\phi}(0.5h)|_{\max}$	11.169	16.750	20.093	21.196	21.714	0

Table 4. Effect of number of electrodes on $\bar{w}$ and $\bar{\phi}$ for cantilever EAM sensory beam (c) ($S = 10$).

Load case	Entity	Number of electrodes					Closed circuit
		1	2	5	10	20	
UDL	$\bar{w}(l, 0)$	−1.8271	−1.8272	−1.8272	−1.8272	−1.8271	−1.8330
	$\bar{\phi}(0.5h)|_{\max}$	−2.3296	−3.4588	−3.8508	−4.2304	−4.5151	0
Tip load	$\bar{w}(l, 0)$	−2.4492	−2.4492	−2.4492	−2.4491	−2.4491	−2.4552
	$\bar{\phi}(0.5h)|_{\max}$	−2.3667	−2.4526	−2.4517	−2.4517	−2.4511	0

Table 5. Effect of number of electrodes on $\bar{w}$ and $\bar{\phi}$ for cantilever SAM sensory beam (d) ($S = 10$).

mode beam, this difference is negligible (0.25–0.3%). The induced sensory potential in the shear mode case is 21 and 11% of the extension mode sensory potential for the UDL and the tip load, respectively.

The undamped natural frequencies of the cantilever sensory EAM beam (c) and SAM beam (d) when the beam surfaces are segmented in to 1, 2, 5, 10 and 20 electroded patches are presented in Table 6 for five modes. All the electrode segments are in open circuit condition. The frequency of the nth mode is nondimensionalized as $\bar{\omega}_n = \omega_n l S (\rho_0 / Y_0)^{1/2}$ where $\rho_0 = 7500$ kg/m³. For comparison, $\bar{\omega}_n$ of the beams with their top surface being under closed circuit condition is also listed in Table 6. It can be seen from Equation (35) that the effective stiffness matrix gets modified by the electromechanical stiffness corresponding to the open circuit potentials Φ_s. Physically, it occurs since a part of the mechanical energy is converted into electric energy through the induced electric potential and results in an increase in the effective stiffness. Thus, the open circuit frequencies are higher than the closed circuit ones, as can be seen from Table 6. Since the degree of constraint of equipotential condition over the electroded surface changes with the number electrode segments, the latter modifies the electromechanical stiffness and consequently the natural frequencies. It is observed that the natural frequencies of the bimorph EAM

Beam	Entity	Open circuit (# of electrodes)					Closed circuit	Combined open-closed
		1	2	5	10	20		
(c)	$\bar{\omega}_1$	5.3281	5.4224	5.4489	5.4529	5.4538	5.1446	5.4367
	$\bar{\omega}_2$	31.209	31.383	32.372	32.527	32.562	30.858	31.761
	$\bar{\omega}_3$	81.605	83.243	84.478	85.103	85.169	81.292	83.093
	$\bar{\omega}_4$	83.781	84.799	85.103	85.158	85.297	83.781	85.169
	$\bar{\omega}_5$	148.09	148.41	150.81	153.59	154.14	147.80	150.63
(d)	$\bar{\omega}_1$	4.5865	4.5871	4.5875	4.5876	4.5877	4.5792	4.5855
	$\bar{\omega}_2$	27.633	27.882	27.913	27.924	27.930	27.593	27.873
	$\bar{\omega}_3$	71.055	71.055	71.055	71.055	71.055	71.055	71.055
	$\bar{\omega}_4$	73.214	73.298	74.697	74.967	75.033	73.137	74.446
	$\bar{\omega}_5$	134.03	134.09	138.51	139.11	139.43	133.88	137.34

Table 6. Effect of number of electrodes on $\bar{\omega}_n$ for cantilever EAM and SAM beams ($S = 10$).

beam with 1 and 20 electrodes differ by 2 and 4% for the first and the fifth modes, respectively. For the SAM beam, the open circuit natural frequencies are little sensitive to the number of electrodes for the first four modes. For the fifth mode, however, the difference between the frequencies of the beam with 1 and 20 electrodes is 4%, similar to the EAM beam. The open circuit frequencies with 20 electrodes differ from the respective closed circuit frequencies by 6 and 4% for the first and fifth modes, for the EAM beam. The corresponding differences for the SAM beam are 0.3 and 4%. For the EAM beam, the lower mode frequencies are generally more sensitive to the electric boundary conditions than the higher mode ones. The reverse is true for the SAM beam. The case of combined open-closed condition with 10 electrodes from the clamped end being under open circuit condition and the remaining 10 under closed circuit condition is also analyzed and the corresponding natural frequencies are presented in the above table. It is observed that the frequencies for this combined case lie in between the corresponding closed circuit and open circuit frequencies (with 20 electrodes).

6.5. *Hybrid SAM-EAM composite beam.* A thin width (plane stress) composite beam (e) with an EAM piezoelectric patch of PZT-5H bonded at the top surface and a SAM patch embedded between two graphite-epoxy composite faces, see Figure 5, is considered next. The beam has a foam core of the same thickness as the SAM patch at the portion where the patch is not present. The material properties of the graphite epoxy and the foam are selected as [Benjeddou et al. 2000; Kapuria and Alam 2006]:

(i) Graphite epoxy:

$$\{Y_1, Y_2, Y_3, G_{12}, G_{23}, G_{31}\} = \{181, 10.3, 10.3, 7.17, 2.87, 7.17\}\,\text{GPa},$$

$$\{v_{12}, v_{13}, v_{23}\} = \{0.28, 0.28, 0.33\}, \quad \rho = 1578\,\text{kg/m}^3$$

(ii) Foam:

$$\{Y, G\} = \{35.3, 12.76\}\,\text{GPa}, \quad \rho = 32\,\text{kg/m}^3.$$

The length of both the PZT patches is taken as $l_p = 0.2l$. The beam is modeled with 50 equal-size elements to obtain converged results. The surfaces of the piezoelectric patches are electroded. Thus all the elements under a patch are connected to one electric node. The beam is analyzed for the following two load cases:

(1) Actuation potential ϕ_0 on the top surface of the EAM or SAM patch with the other piezoelectric surfaces grounded.

(2) Uniform pressure p_0 applied on the top surface over a length of $l/25$ from the free end. For this load case, the top surface of either EAM or SAM patch is under open circuit condition, while the other piezoelectric surfaces are grounded.

The static results for the two load cases and the natural frequencies are nondimensionalized as

(1) $\bar{w} = 10w/S^2 d_0\phi_0, \qquad \bar{\sigma}_x = \sigma_x h/10Y_0 d_0\phi_0,$

(2) $\bar{\phi} = 10^4\phi Y_0 d_0/hS^2 p_0, \qquad \bar{\omega}_n = \omega_n l S(\rho_0/Y_0)^{1/2},$

with $Y_0 = 6.9\,\text{GPa}$, $d_0 = 274.8 \times 10^{-12}\,\text{CN}^{-1}$ and $\rho_0 = 1000\,\text{kg/m}^3$.

In order to illustrate the effect of location x_p of the EAM and SAM actuators on their actuation capability, one of the actuators (EAM or SAM) is actuated with electric potential of load case 1 and its

	Potential load						Pressure load	
	EAM			SAM			EAM	SAM
x_p/l	$\bar{w}(l,0)$	$\bar{\sigma}_x^p(x_p,0.5h^+)$	$\bar{\sigma}_x^e(x_p,0.5h^-)$	$\bar{w}(l,0)$	$\bar{\sigma}_x^p(x'_p,0.05h^-)$	$\bar{\sigma}_x^e(x'_p,-0.5h)$	$\bar{\phi}(0.6h)$	$\bar{\phi}(0.05h)$
0.1	−5.012	−6.881	3.970	−1.358	0.6902	−1.167	−1.899	−0.1381
0.3	−3.982	−6.864	4.053	−1.496	0.2748	−1.303	−1.496	−0.1953
0.5	−2.821	−6.863	4.055	−1.122	0.2748	−1.303	−1.046	−0.1953
0.7	−1.693	−6.863	4.055	−0.7474	0.2748	−1.303	−0.6101	−0.1953
0.9	−0.5598	−6.863	4.057	−0.3718	0.2748	−1.303	−0.1802	−0.1851

Table 7. Effect of actuator/sensor location on the response of hybrid beam (e) ($S = 20$). Here, $x'_p = x_p - 0.5l_p$, x_p denotes x_e for EAM and x_s for SAM.

location is varied from the clamped end ($x_p = 0.1l$) to the free end ($x_p = 0.9l$), while the unactuated patch is kept fixed at the clamped end. x_p refers to x_e for the EAM and x_s for the SAM, see Figure 5. The tip deflection $\bar{w}$, axial stress $\bar{\sigma}_x^e$ in the elastic substrate and $\bar{\sigma}_x^p$ in the actuated piezoelectric patch are presented in Table 7 for the beam with $S = 20$ for both EAM and SAM actuation cases for five different actuator locations. The tip deflection is also plotted against the actuator location in Figure 14. It is observed that the EAM actuator is most effective inducing the maximum deflection, when placed at the clamped end. The SAM actuator develops the maximum tip deflection when it is placed at a clear distance of $0.1l$ from the clamped end ($x_p = 0.2l$).

This observation is in line with the results of Sun and Zhang [1995] obtained for Al/PZT-5H beams, through 2D FE analysis. It, however, does not support the conclusion made by Raja et al. [2004] based on the three-layer sandwich model that the shear actuator for a cantilever beam is most effective if it is placed at the center of the beam. It is revealed from Table 7 that even though the maximum tip deflection developed by shear actuator is 36% of that produced by the extension mode actuator, the maximum stress $\bar{\sigma}_x^p$ induced in the actuator for the SAM is only 10% of that for the EAM. Also, the maximum value of $\bar{\sigma}_x^e$ induced in the elastic substrate for SAM is 29% of that for EAM. Thus, for the same stress level in
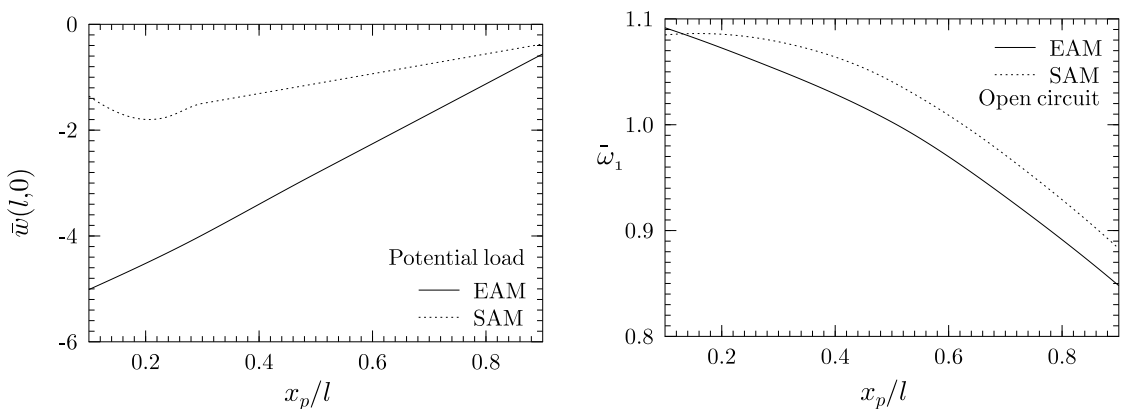

Figure 14. Variation of tip deflection and natural frequency of hybrid beam (e) with actuator/sensor location.
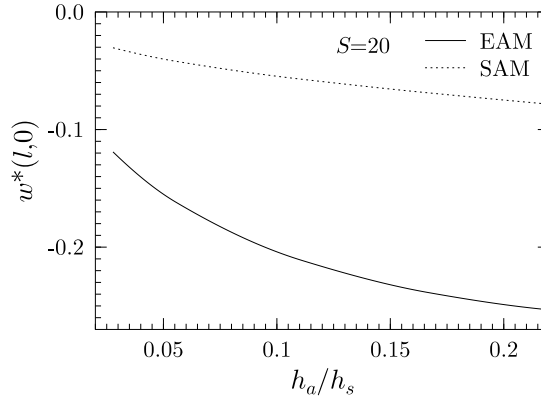
Figure 15. Variation of tip deflection with actuator thickness for actuation with constant energy for hybrid beam (e).

the actuator (which is often the governing criteria), the SAM actuator can develop more tip deflection than the EAM actuator. This is an attractive feature of the SAM actuators, which can be useful in many control applications.

The sensory potential developed when the beam is subjected to mechanical load of case (2) is also presented in Table 7 for different locations of the SAM and EAM sensors. It is revealed that for the extension mode, the sensor is most effective when placed at the clamped end like the actuator. For the shear mode, however, the sensory potential for this tip loading case is independent of the location beyond a small distance from the the clamped end. As explained earlier, this is because the sensory potential is related to the induced shear which is constant in the region $0 \leq x \leq 0.96l$, for the present loading.

The variation of the fundamental frequency $\bar{\omega}_1$ of the hybrid beam (e) with the location of the EAM and SAM sensors is plotted in Figure 14. As expected, the frequency of the beam reduces as the sensor is moved from the clamped to the free end. This reduction is more for the surface mounted patch than the embedded one.

6.6. *Effect of actuator thickness on actuation capability.* Here the entities are nondimensionalized as $w^* = 1000w/h$, $\phi^* = \phi d_0/h$. The energy required to develop a potential difference ϕ_0^* across an actuator of thickness h_a for the beam (e) with thickness of the composite substrate being h_s is proportional to $E_v = \phi_0^{*2}/(h_a/h_s)$. To illustrate the effect of actuator thickness on its effectiveness, the actuator potential is varied for varying h_a such that E_v is constant ($= 10^{-11}$). The induced deflection w^* is plotted as a function h_a/h_s in Figure 15 for both SAM and EAM actuators. It is observed that in both cases, the actuation authority increases with the increase in h_a/h_s. However, the rate of increase in w^* reduces with the increase in h_a/h_s.

7. Conclusions

The new unified formulation based on the efficient layerwise approximations for the displacement field and sublayerwise quadratic approximation for the electric potential can model actuators, sensors and hybrid adaptive beams with surface-mounted and embedded actuator/sensor patches in extension or shear

mode. The numerical results show that the model accurately predicts the nonuniform variation of w across the thickness in presence of electric field, and also the quadratic and cubic variations of electric potential in the extension and shear modes, respectively, as observed from 2D piezoelasticity solutions. The concept of electric node results in significant reduction in the number of electric DOF.

It is revealed that while for the extension mode sensor, the sensory potential is dependent on the sensor location unless the loading causes a constant bending moment, the sensory potential in shear mode does not change with the location, if the loading causes constant shear. For extension mode sensors, the number of segments in the electroded surface can have appreciable effect on the deflection and natural frequencies. However, for the shear mode sensors, the deflection and lower mode natural frequencies are independent of the segmentation of the electrode. An extension actuator yields maximum tip deflection in a cantilever adaptive beam when it is placed at the clamped end, whereas a shear actuator should be placed at a distance of $l/10$ from the clamped end to develop the maximum tip deflection. The ability of an actuator in inducing deflection for a given energy increases with its thickness for both extension and shear mode actuation.

Appendix

The transformation matrices a, T and R in Equation (2) are given by

$$
R = \begin{bmatrix}
1 & 0 & 0 & 0 & 0 & 0 \\
0 & 1 & 0 & 0 & 0 & 0 \\
0 & 0 & 1 & 0 & 0 & 0 \\
0 & 0 & 0 & 2 & 0 & 0 \\
0 & 0 & 0 & 0 & 2 & 0 \\
0 & 0 & 0 & 0 & 0 & 2
\end{bmatrix},
\quad
T = \begin{bmatrix}
c^2 p^2 & s^2 p^2 & q^2 & 2spq & 2cpq & 2csp^2 \\
s^2 & c^2 & 0 & 0 & 0 & -2cs \\
c^2 q^2 & s^2 q^2 & p^2 & -2spq & -2cpq & 2csq^2 \\
csq & -csq & 0 & cp & -sp & -(c^2 - s^2)q \\
-c^2 pq & -s^2 pq & pq & s(p^2 - q^2) & c(p^2 - q^2) & -2cspq \\
-csp & csp & 0 & cq & -sq & (c^2 - s^2)p
\end{bmatrix},
$$

$$
a = \begin{bmatrix}
cq & sp & q \\
-s & c & 0 \\
-cp & -sq & p
\end{bmatrix},
$$

where $c = \cos\alpha$, $s = \sin\alpha$, $p = \cos\beta$, and $q = \sin\beta$. The expressions of $\bar{s}_{ij}$, $\bar{d}_{ij}$ and $\bar{\epsilon}_{ij}$ in Equation (5) are given, for the case $pq = 0$, by

$$
\bar{s}_{11} = c^4 p^4 s_{11} + c^2 s^2 p^2 (2s_{12} + s_{66}) + s^4 s_{22} + c^2 s^2 q^2 (2s_{23} + s_{44}) + c^4 q^4 s_{33},
$$

$$
\bar{s}_{55} = s^2 p^2 s_{44} + c^2 (p^4 + q^4) s_{55} + s^2 q^2 s_{66},
$$

$$
\bar{d}_{11} = -cq[s^2(d_{32} + d_{24}) + c^2 q^2 d_{33}], \qquad \bar{d}_{35} = -cq^3 d_{15},
$$

$$
\bar{d}_{31} = p(c^2 p^2 d_{31} + s^2 d_{32}), \qquad \bar{d}_{15} = p(c^2 p^2 d_{15} + s^2 d_{24}),
$$

$$
\bar{\epsilon}_{11} = c^2 p^2 \epsilon_{11} + s^2 \epsilon_{22} + c^2 q^2 \epsilon_{33}, \qquad \bar{\epsilon}_{33} = q^2 \epsilon_{11} + p^2 \epsilon_{33}.
$$

The expressions of $\bar{c}_{ij}$, $\bar{e}_{ij}$ and $\bar{\eta}_{ij}$ in Equation (8) are given, for the case $pq = 0$, by

$$\bar{c}_{11} = c^4 p^4 c_{11} + 2c^2 s^2 p^2 (c_{12} + 2c_{66}) + s^4 c_{22} + 2c^2 s^2 q^2 (c_{23} + 2c_{44}) + c^4 q^4 c_{33},$$

$$\bar{c}_{13} = s^2 p^2 c_{23} + c^2 (p^4 + q^4) c_{13} + s^2 q^2 c_{12}, \qquad \bar{c}_{33} = q^4 c_{11} + p^4 c_{33},$$

$$\bar{c}_{55} = s^2 p^2 c_{44} + c^2 (p^4 + q^4) c_{55} + s^2 q^2 c_{66},$$

$$\bar{e}_{11} = -cq[s^2(e_{32} + 2e_{24}) + c^2 q^2 e_{33}], \qquad \bar{e}_{35} = -cq^3 e_{15},$$

$$\bar{e}_{31} = p(c^2 p^2 e_{31} + s^2 e_{32}), \qquad \bar{e}_{15} = p(c^2 p^2 e_{15} + s^2 e_{24}),$$

$$\bar{\eta}_{11} = c^2 p^2 \eta_{11} + s^2 \eta_{22} + c^2 q^2 \eta_{33}, \qquad \bar{\eta}_{33} = q^2 \eta_{11} + p^2 \eta_{33}.$$

The hatted R-coefficients in Equation (12) are defined as $\{\hat{R}_1^k, \hat{R}_2^k, \hat{R}_3, \hat{R}_4\} = \{R_1^k, R_2^k, R_3, R_4\}/R_2^{k0}$ with

$$R_1^k = \bar{R}_2^k - \bar{R}_2^{k0}, \quad R_2^k = a_1^k R_3 + a_2^k R_4, \quad R_3 = \frac{4C_2^L}{\Delta}, \quad R_4 = -\frac{4C_1^L}{3\Delta}, \quad \bar{R}_2^k = \sum_{i=2}^{k} z_{i-1}(R_2^{i-1} - R_2^i),$$

$$a_1^k = 2(C_1^k/\hat{Q}_{55}^k - z_k), \qquad a_2^k = 3(2C_2^k/\hat{Q}_{55}^k - z_k^2), \qquad \Delta = 4z_0^2 C_1^L - 8z_0 C_2^L,$$

$$C_1^k = \sum_{i=1}^{k} \hat{Q}_{55}^i (z_i - z_{i-1}), \qquad C_2^k = \tfrac{1}{2} \sum_{i=1}^{k} \hat{Q}_{55}^i (z_i^2 - z_{i-1}^2).$$

Using Equations (18), (23), (24), (27), (29) and (30), the elements of the submatrices of M^e, C^e and K^e defined in Equation (31) are obtained by exact integration as

$$M_{uu}^e = \begin{bmatrix} I_{11}c_1 & -I_{12}c_2 & I_{13}c_1 \\ & I_{22}c_3 + I_{11}c_4 & -I_{23}c_2^{\mathrm{T}} \\ \text{symm.} & & I_{33}c_1 \end{bmatrix}, \qquad C_{uu}^e = \begin{bmatrix} 0 & 0 & 0 \\ & \hat{c}_1 c_4 & 0 \\ \text{symm.} & & 0 \end{bmatrix},$$

$$K_{uu}^e = \begin{bmatrix} A_{11}c_5 & -A_{12}c_6 & A_{13}c_5 \\ & A_{22}c_7 & -A_{23}c_6^{\mathrm{T}} \\ \text{symm.} & & A_{33}c_5 + \bar{A}_{11}c_1 \end{bmatrix}, \qquad K_{ul}^e = \begin{bmatrix} e_1^{1l'}c_5 + e_{11}^{2l'}c_8 \\ -(e_2^{1l'}c_6^{\mathrm{T}} + e_{12}^{2l'}c_{10}) \\ e_3^{1l'}c_5 + e_{13}^{2l'}c_8 + (e_1^{3l'} - \bar{A}_{12}^{l'})c_8^{\mathrm{T}} + e_{11}^{4l'}c_1 \end{bmatrix},$$

$$K_{uj}^e = \begin{bmatrix} e_{21}^{2j'}c_9 \\ -e_{22}^{2j'}c_{11} \\ e_{23}^{2j'}c_9 + e_{21}^{4j'}c_{12} \end{bmatrix}, \qquad K_{lj}^e = \begin{bmatrix} -(\delta_1 e_{22}^{4lj'} + \eta_2^{2lj'})c_9 - \eta_{12}^{3lj'}c_{12} \end{bmatrix},$$

$$K_{ll}^e = \begin{bmatrix} (\bar{A}_{22}^{ll'} - 2\delta_1 e_2^{3ll'} - \eta_1^{ll'})c_5 - (\delta_1 e_{12}^{4ll'} + \eta_1^{2ll'})(c_8 + c_8^{\mathrm{T}}) - \eta_{11}^{3ll'}c_1 \end{bmatrix},$$

$$K_{jj}^e = \begin{bmatrix} -\eta_{22}^{3jj'}a \end{bmatrix},$$

where c_i are given by

$$c_1 = \int_0^a N^T N \, dx = \frac{a}{3} \begin{bmatrix} 1 & 1/2 \\ 1/2 & 1 \end{bmatrix},$$

$$c_2 = \int_0^a N^T \bar{N}_{,x} \, dx = \frac{1}{2} \begin{bmatrix} -1 & a/6 & 1 & -a/6 \\ -1 & -a/6 & 1 & a/6 \end{bmatrix},$$

$$c_3 = \int_0^a \bar{N}_{,x}^T \bar{N}_{,x} \, dx = \begin{bmatrix} 6/5a & 1/10 & -6/5a & 1/10 \\ 1/10 & 2a/15 & -1/10 & -a/30 \\ -6/5a & -1/10 & 6/5a & -1/10 \\ 1/10 & -a/30 & -1/10 & 2a/15 \end{bmatrix},$$

$$c_4 = \int_0^a \bar{N}^T \bar{N} \, dx = \begin{bmatrix} 13a/35 & 11a^2/210 & 9a/70 & -13a^2/420 \\ 11a^2/210 & a^3/105 & 13a^2/420 & -a^3/140 \\ 9a/70 & 13a^2/420 & 13a/35 & -11a^2/210 \\ -13a^2/420 & -a^3/140 & -11a^2/210 & a^3/105 \end{bmatrix},$$

$$c_5 = \int_0^a N_{,x}^T N_{,x} \, dx = \frac{1}{a} \begin{bmatrix} 1 & -1 \\ -1 & 1 \end{bmatrix},$$

$$c_6 = \int_0^a N_{,x}^T \bar{N}_{,xx} \, dx = \frac{1}{a} \begin{bmatrix} 0 & 1 & 0 & -1 \\ 0 & -1 & 0 & 1 \end{bmatrix},$$

$$c_7 = \int_0^a \bar{N}_{,xx}^T \bar{N}_{,xx} \, dx = \begin{bmatrix} 12/a^3 & 6/a^2 & -12/a^3 & 6/a^2 \\ 6/a^2 & 4/a & -6/a^2 & 2/a \\ -12/a^3 & -6/a^2 & 12/a^3 & -6/a^2 \\ 6/a^2 & 2/a & -6/a^2 & 4/a \end{bmatrix},$$

$$c_8 = \int_0^a N_{,x}^T N \, dx = \frac{1}{2} \begin{bmatrix} -1 & -1 \\ 1 & 1 \end{bmatrix},$$

$$c_9 = \int_0^a N_{,x}^T \, dx = \begin{bmatrix} -1 \\ 1 \end{bmatrix},$$

$$c_{10} = \int_0^a \bar{N}_{,xx}^T N \, dx = \begin{bmatrix} -1/a & 1/a \\ -1 & 0 \\ 1/a & -1/a \\ 0 & 1 \end{bmatrix},$$

$$c_{11} = \int_0^a \bar{N}^{\mathrm{T}}_{,xx} \, dx = \begin{bmatrix} 0 \\ -1 \\ 0 \\ 1 \end{bmatrix},$$

$$c_{12} = \int_0^a N^{\mathrm{T}} \, dx = \frac{a}{2} \begin{bmatrix} 1 \\ 1 \end{bmatrix}.$$

Considering that the loading terms p_z^1, p_z^2, D_{z_0}, D_{z_L} vary linearly over the length of the element with nodal values

$$p_z^{1^e}, \, p_z^{2^e}, \, D_{z_0}^e, \, D_{z_L}^e$$

via the relation $p_z^i = N p_z^{i^e}$, $D_{z_i} = N D_{z_i}^e$, the elements of P_u^e and P_j^e in Equation (31) are obtained as

$$P_u^e = \begin{bmatrix} 0 \\ c_{13} p_z^e \\ 0 \end{bmatrix}, \qquad P_j^e = \begin{bmatrix} b c_{12}^{\mathrm{T}} p_\phi^{j^e} \end{bmatrix},$$

where

$$c_{13} = b \int_0^a \bar{N}^{\mathrm{T}} N \, dx = \frac{b}{10} \begin{bmatrix} 7a/2 & 3a/2 \\ a^2/2 & a^2/3 \\ 3a/2 & 7a/2 \\ -a^2/3 & -a^2/2 \end{bmatrix},$$

$$p_z^e = p_z^{1^e} + p_z^{2^e},$$

$$p_\phi^{j^e} = -\delta_1 \big[p_z^{1^e} \bar{\Psi}_\phi^j(z_0) + p_z^{2^e} \bar{\Psi}_\phi^j(z_L) \big] - D_{z_0}^e \delta_{j1} + D_{z_L}^e \delta_{jn_\phi}.$$

References

[Aldraihem and Khdeir 2003] O. J. Aldraihem and A. A. Khdeir, "Exact deflection solutions of beams with shear piezoelectric actuators", *Int. J. Solids Struct.* **40**:1 (2003), 1–12.

[Auld 1973] B. A. Auld, *Acoustic fields and waves in solids*, vol. 1, Wiley, New York, 1973.

[Benjeddou 2000] A. Benjeddou, "Advances in piezoelectric finite element modeling of adaptive structural elements: a survey", *Comput. Struct.* **76**:1-3 (2000), 347–363.

[Benjeddou et al. 1997] A. Benjeddou, M. A. Trindade, and R. Ohayon, "A unified beam finite element model for extension and shear piezoelectric actuation mechanisms", *J. Intell. Mater. Syst. Struct.* **8**:12 (1997), 1012–1025.

[Benjeddou et al. 1999] A. Benjeddou, M. A. Trindade, and R. Ohayon, "New shear actuated smart structure beam finite element", *AIAA J.* **37**:3 (1999), 378–383.

[Benjeddou et al. 2000] A. Benjeddou, M. A. Trindade, and R. Ohayon, "Piezoelectric actuation mechanisms for intelligent sandwich structures", *Smart Mater. Struct.* **9** (2000), 328–335.

[Bisegna and Caruso 2001] P. Bisegna and G. Caruso, "Evaluation of higher-order theories of piezoelectric plates in bending and in stretching", *Int. J. Solids Struct.* **38**:48-49 (2001), 8805–8830.

[Chandrupatla and Belegundu 2002] T. R. Chandrupatla and A. D. Belegundu, *Introduction to finite elements in engineering*, Pearson Education (Singapore) Pte Ltd., New Delhi, 2002.

[Correia et al. 2000] V. M. F. Correia, M. A. A. Gomes, A. Suleman, C. M. M. Soares, and C. A. M. Soares, "Modelling and design of adaptive composite structures", *Comput. Methods Appl. Mech. Eng.* **185**:2-4 (2000), 325–346.

[Dube et al. 1996] G. P. Dube, S. Kapuria, and P. C. Dumir, "Exact piezothermoelastic solution of simply-supported orthotropic flat panel in cylindrical bending", *Int. J. Mech. Sci.* **38**:11 (1996), 1161–1177.

[Gopinathan et al. 2000] S. V. Gopinathan, V. V. Varadan, and V. K. Varadan, "A review and critique of theories for piezoelectric laminates", *Smart Mater. Struct.* **9**:1 (2000), 24–48.

[Kapuria 2001] S. Kapuria, "An efficient coupled theory for multilayered beams with embedded piezoelectric sensory and active layers", *Int. J. Solids Struct.* **38**:50-51 (2001), 9179–9199.

[Kapuria and Alam 2006] S. Kapuria and N. Alam, "Efficient layerwise finite element model for dynamic analysis of laminated piezoelectric beams", *Comput. Methods Appl. Mech. Eng.* **195**:19-22 (2006), 2742–2760.

[Kapuria et al. 1997] S. Kapuria, G. P. Dube, and P. C. Dumir, "Exact piezothermoelastic solution for simply supported laminated flat panel in cylindrical bending", *Z. Angew. Math. Mech.* **77**:4 (1997), 281–293.

[Kapuria et al. 2003] S. Kapuria, P. C. Dumir, and A. Ahmed, "An efficient coupled layerwise theory for static analysis of piezoelectric sandwich beams", *Arch. Appl. Mech.* **73**:3-4 (2003), 147–159.

[Khdeir and Aldraihem 2001] A. A. Khdeir and O. J. Aldraihem, "Deflection analysis of beams with extension and shear piezoelectric patches using discontinuity functions", *Smart Mater. Struct.* **10**:2 (2001), 212–220.

[Lage et al. 2004] R. G. Lage, C. M. M. Soares, C. A. M. Soares, and J. N. Reddy, "Modelling of piezolaminated plates using layerwise mixed finite elements", *Comput. Struct.* **82**:23-26 (2004), 1849–1863.

[Lee and Saravanos 1996] H. J. Lee and D. A. Saravanos, "Coupled layer-wise analysis of thermopiezoelectric composite beams", *AIAA J.* **34**:6 (1996), 1231–1237.

[Parashar et al. 2004] S. K. Parashar, U. von Wagner, and H. P., "A modified Timoshenko beam theory for nonlinear shear-induced flexural vibrations of piezoceramic continua", *Nonlinear Dyn.* **37**:3 (2004), 181–205.

[Parashar et al. 2005] S. K. Parashar, U. von Wagner, and H. P., "Nonlinear shear-induced flexural vibrations of piezoceramic actuators: experiments and modeling", *J. Sound Vib.* **285**:4-5 (2005), 989–1014.

[Petyt 1990] M. Petyt, *Introduction to finite element vibration analysis*, Cambridge University Press, Cambridge, 1990.

[Plagianakos and Saravanos 2005] T. S. Plagianakos and D. A. Saravanos, "Coupled high-order shear layerwise analysis of adaptive sandwich piezoelectric composite beams", *AIAA J.* **43**:4 (2005), 885–894.

[Raja et al. 2002] S. Raja, G. Prathap, and P. K. Sinha, "Active vibration control of composite sandwich beams with piezoelectric extension-bending and shear actuators", *Smart Mater. Struct.* **11**:1 (2002), 63–71.

[Raja et al. 2004] S. Raja, R. Sreedeep, and G. Prathap, "Bending behavior of hybrid-actuated piezoelectric sandwich beams", *J. Intell. Mater. Syst. Struct.* **15**:8 (2004), 611–619.

[Robbins and Reddy 1991] D. H. Robbins and J. N. Reddy, "Analysis of piezoelectrically actuated beams using a layer-wise displacement theory", *Comput. Struct.* **41**:2 (1991), 265–279.

[Saravanos 1999] D. A. Saravanos, "Damped vibration of composite plates with passive piezoelectric-resistor elements", *J. Sound Vib.* **221**:5 (1999), 867–885.

[Saravanos and Heyliger 1999] D. A. Saravanos and P. R. Heyliger, "Mechanics and computational models for laminated piezoelectric beams plates and shells", *Appl. Mech. Rev.* **52** (1999), 305–320.

[Saravanos et al. 1997] D. A. Saravanos, P. R. Heyliger, and D. A. Hopkins, "Layerwise mechanics and finite element for the dynamic analysis of piezoelectric composite plates", *Int. J. Solids Struct.* **34**:3 (1997), 359–378.

[Shu and Sun 1994] X. Shu and L. Sun, "An improved simple higher order theory for laminated composite plates", *Comput. Struct.* **50**:2 (1994), 231–236.

[Sun and Zhang 1995] C. T. Sun and X. D. Zhang, "Use of thickness-shear mode in adaptive sandwich structures", *Smart Mater. Struct.* **4**:3 (1995), 202–206.

[Sze and Yao 2000] K. Y. Sze and L. Q. Yao, "Modelling smart structures with segmented piezoelectric sensors and actuators", *J. Sound Vib.* **235**:3 (2000), 495–520.

[Sze et al. 2004] K. Y. Sze, X.-M. Yang, and H. Fan, "Electric assumptions for piezoelectric laminate analysis", *Int. J. Solids Struct.* **41**:9-10 (2004), 2363–2382.

[Tiersten 1969] H. F. Tiersten, *Linear piezoelectric plate vibrations*, Plenum Publishing Corporation, New York, 1969.

[Trindade and Benjeddou 2005] M. A. Trindade and A. Benjeddou, "Refined sandwich finite element model for smart beams with shear piezoceramic actuators and sensors", in *Proceedings of II Eccomas Thematic Conference on Smart Structures and Materials*, vol. 1-20, Lisbon, Portugal, 2005.

[Tzou and Tseng 1990] H. Tzou and C. I. Tseng, "Distributed piezoelectric sensor/actuator design for dynamic measurement/control of distributed parameter systems: a piezoelectric finite element approach", *J. Sound Vib.* **138**:1 (1990), 17–34.

[Vasques and Rodrigues 2005] C. M. A. Vasques and J. D. Rodrigues, "Coupled three-layered analysis of smart piezoelectric beams with different electric boundary conditions", *Int. J. Numer. Methods Eng.* **62**:11 (2005), 1488–1518.

[Wang 2004] S. Y. Wang, "A finite element model for the static and dynamic analysis of a piezoelectric bimorph", *Int. J. Solids Struct.* **41**:15 (2004), 4075–4096.

[Zhang and Sun 1996] X. D. Zhang and C. T. Sun, "Formulation of an adaptive sandwich beam", *Smart Mater. Struct.* **5**:6 (1996), 814–823.

SANTOSH KAPURIA: kapuria@am.iitd.ac.in
Dynamics and Vibrations Group, Department of Mechanical Engineering, Technische Universität Darmstadt, Hochschulstrasse 1, 64289 Darmstadt, Germany

PETER HAGEDORN: peter.hagedorn@dyn.tu-darmstadt.de
Dynamics and Vibrations Group, Department of Mechanical Engineering, Technische Universität Darmstadt, Hochschulstrasse 1, 64289 Darmstadt, Germany